Rare-Earth Doped Aluminum Oxide Lasers for Silicon Photonics

by

Emir Salih Magden

Submitted to the Department of Electrical Engineering and Computer Science
in partial fulfillment of the requirements for the degree of

Master of Science in Electrical Engineering and Computer Science

at the

MASSACHUSETTS INSTITUTE OF TECHNOLOGY
June 2014

© Massachusetts Institute of Technology 2014. All rights reserved.

Author...
Department of Electrical Engineering and Computer Science
May 21, 2014

Certified by ....
Leslie A. Kolodziejski
Professor of Electrical Engineering
Thesis Supervisor

Accepted by ....
Leslie A. Kolodziejski
Chairman, Department Committee on Graduate Students

Rare-Earth Doped Aluminum Oxide Lasers for Silicon Photonics

by

Emir Salih Magden

Submitted to the Department of Electrical Engineering and Computer Science on May 21, 2014 in partial fulfillment of the requirements for the degree of Master of Science in Electrical Engineering and Computer Science

Abstract

A reliable and CMOS-compatible deposition process for amorphous Al_2O_3 based active photonic components has been developed. Al_2O_3 films were reactively sputtered, where process optimization was achieved at a temperature of 250 °C, with a deposition rate of 8.5 nm/min. With a surface roughness of 0.3 nm over a 1 μm^2 area, background optical losses as low as 0.1 dB/cm were obtained for undoped films. The development of active photonics components has been realized by use of rare-earth metals as dopants. By co-sputtering aluminum and erbium targets, Er^{3+} dopants at concentrations on the order of 1.0×10^{20} cm^{-3} have been added to the Al_2O_3 host medium. Resulting Er^{3+}:Al_2O_3 films have been characterized, and over 3 dB/cm absorption has been measured over a 20 nm bandwidth. Following the material development, distributed Bragg reflector lasers were designed and fabricated in a CMOS foundry. The laser cavity was created by introducing gratings on either side of a Si_3N_4 waveguide. Er^{3+}:Al_2O_3 was deposited in SiO_2 trenches on top of the Si_3N_4 layer, eliminating the need for any subsequent etching steps. On-chip laser output of 3.9 μW has been recorded at a wavelength of 1533.4 nm, with a side mode suppression ratio over 38.9 dB.

Thesis Supervisor: Leslie A. Kolodziejski
Title: Professor of Electrical Engineering and Computer Science

Acknowledgements

My master's degree adventures throughout last two years had so many ups and downs that these two years now feel like one of the biggest roller-coaster rides of my life. It only seems appropriate to start this thesis by thanking those who have helped me through this ride during its best and worst times.

First and foremost, I must thank my advisor Prof. Leslie Kolodziejski, for none of this would have been possible without her support and guidance. From day one, she has not only helped me navigate through experiments, but also took the time to teach me how to become an efficient and skilled researcher, which extends far beyond the work in the lab. Day by day, I realize how important these skills are, and am thankful that I had the opportunity of working with such a wonderful advisor who continually made sure I knew there was more to doing research than just lab work and simulations. I have also learned a great deal from Dr. Gale Petrich who helped me with his expertise through many depositions which directly led to the results in this thesis. I am therefore grateful to have had a chance to work with him, and for his detailed and accurate answers to all my questions.

I would also like to thank Prof. Michael Watts whose group I have been working with for the last year. Without his support and the vision from his group, the work in this thesis would not have found such appropriate applications. I am especially pleased to have had many chances to consult Erman Timurdogan, Zhan Su, Dr. Jie Sun, Dr. Ehsan Shah Hosseini, Dr. Jonathan Bradley, Dr. Michele Moresco, Dr. Gurpreet Singh, Purnawirman, Dr. Anna Baldycheva, David Cole, Ami Yaacobi, Cheryl Sorace-Agaskar, Patrick Callahan, and Harneet Khurana, who have helped me understand concepts and design techniques time and time again.

This work would also not have been possible without the expertise of the Nanostructures Laboratory (NSL), Microsystems Technology Laboratories (MTL), and Center for Materials Science and Engineering (CMSE) staff. I would like to specifically thank Dr. Vicky Diadiuk, Scott Poesse, Kurt Broderick, Jim Daley, Dr. Euclid Moon, Elisabeth Shaw, and Dennis Ward, due to their immense contributions to my fabrication and metrology knowledge.

I am grateful to my parents and grandparents, for their eternal support, love, and everything they have done for me. Their encouragement and continued faith in me played an extremely important role in where I am today. I am thankful for not only the things they have done for me, but also what they

enabled me to do on my own. This thesis would not have been possible if it weren't for the values they have taught me since my early childhood.

Finally, I like to express my sincerest gratitude my girlfriend Zeynep who has supported me in all my endeavors, and helped me push through the toughest times during my thesis work.

Emir Salih Magden
Cambridge 2014

Financial Support

This work in this thesis was supported in part by the Defense Advanced Research Projects Agency (DARPA) Microsystems Technology Office's (MTO) EPHI program, grant no. HR0011-12-2-0007.

dedicated to my parents
Abdullah Mağden
and
Nurcan Mağden

CONTENTS

10 LIST OF FIGURES
12 LIST OF TABLES

13 **1 MOTIVATION FOR SILICON PHOTONICS**
14 **1.1** Why Integrate Optics With CMOS Technology?
19 **1.2** Integrated Laser Solutions
20 **1.3** Erbium Doped Amorphous Aluminum Oxide (Er^{3+}:Al_2O_3)

24 **2 FABRICATION METHODOLOGY AND MATERIAL CHARACTERIZATION**
25 **2.1** Advantages of Sputtering
25 **2.2** The Kurt J. Lesker Lab 18 Sputtering Tool
28 **2.3** Sputtering Process Optimization for Low-Loss Al_2O_3 and Uniformly Doped Er^{3+}:Al_2O_3
28 **2.3.1** Standard Operating Procedure for Lab 18
30 **2.3.2** Determining the Optimum Deposition Conditions for Low-Loss Al_2O_3
37 **2.3.3** Characterization of Dopant Concentration

41 **3 INTEGRATED DISTRIBUTED BRAGG REFLECTOR LASER DESIGN AND OPERATION**
42 **3.1** Design Considerations for Optically-Pumped On-Chip Lasers
43 **3.2** Design of On-Chip Distributed Bragg Reflector (DBR) Laser
43 **3.2.1** Laser Cavity Design
47 **3.2.2** Spectral Response of Distributed Bragg Reflectors
51 **3.3** Fabrication and Measurement of On-Chip DBR Lasers

56 **4 CONCLUSIONS AND OUTLOOK**
57 **4.1** Summary and Conclusions
58 **4.2** Future Work and Outlook

61 REFERENCES

LIST OF FIGURES

1.1 Scaling trends for transistor gate length (known as Dennard's Law) from 1970 to the projected node sizes of 2020 14

1.2 Scaling trends for processor clock frequency from numerous manufacturers since 1985. Clock frequency clearly levels off around 3-4 GHz after 2003 15

1.3 3D integration schemes for addressing the communication bottleneck: (a) GPU chip with ball-grid array, (b) logic and memory integration using through-silicon-vias (concept) 16

1.4 Schematic diagram of on-chip silicon photonics link featuring wavelength division multiplexed laser array, multiplexers, demultiplexers, modulators, and detectors 17

1.5 Collection of passive optical devices on-chip: (a) modulator, (b) multiplexer, (c) waveguide, (d) detector. 18

1.6 Optical losses per unit length of silica fiber. Influences by Rayleigh scattering at shorter wavelengths, and infrared vibrational losses are clearly observed. Absorption peaks of OH^- ions are not shown, as they can be eliminated under proper deposition conditions. 21

1.7 Energy diagram and commonly used transitions of erbium ion Er^{3+} 22

1.8 (a) Absorption and (b) Emission cross-section spectra of Er^{3+} between 1.4 μm and 1.7 μm 23

2.1 Kurt J. Lesker Lab 18 sputtering system located in NanoPrecision Deposition Laboratory at MIT 26

2.2 Water vapor partial pressure inside the process chamber (light blue), and substrate temperature (dark blue) during outgas. After the substrate temperature is held at 400 °C for two hours, water pressure has dropped to levels similar to what it was before the outgas. 29

2.3 Discharge voltage developed across the Al target as a function of (a) the ratio of O_2 flow to Ar flow, and (b) O_2 flow. Dark blue indicates measurements under constant Ar flow of 160 sccm, whereas light blue is used to display discharge voltage measured at a constant pressure of 3 mT. Both sets of measurements are taken with maximum pumping speed possible. 31

2.4 Variation in the current supplied to the substrate heater during ramp-up 33

from room temperature to 400 ºC for 6” and 8” substrates, and 20 x 25 mm chips

2.5 Optical losses of reactively sputtered Al_2O_3 films as a function of substrate temperature during deposition. Other deposition conditions such as pressure, RF power delivered to the substrate and the Al target, and O_2 flow are kept constant at 5 mT, 90 W, 400 W, and 4.1 sccm, respectively. 34

2.6 Optical losses of reactively sputtered Al_2O_3 films as a function of substrate bias. Other deposition conditions such as pressure, substrate temperature, RF power delivered to the Al target, and the O_2 flow are kept constant at 5 mT, 250 ºC, 400 W, and 4.1 sccm respectively. 35

2.7 Atomic force micrographs of films deposited with (a) no substrate bias, (b) 90 W substrate bias over 1μm^2 area. Root mean square surface roughness has significantly decreased, with the addition of 90 W substrate bias. Note the vertical scale differences between the two surfaces, indicating the magnitude of the difference between the surface roughness of the two samples. 36

2.8 Behavior of erbium discharge voltage under 30 W and 45 W constant RF power (solid lines), and the amount of power required to keep stable erbium discharge voltage of 60 V and 75 V (dotted and dashed lines). 38

2.9 Absorption losses in the pump and signal wavelengths of Er^{3+}:Al_2O_3 films doped with Er^{3+} discharge voltages of (a) 60 V and (b) 75 V. Absorption cross-section data of Er^{3+} is plotted on the secondary vertical axes with the solid line. Concentrations of 9.5x10^{19} cm^{-3} and 1.9x10^{20} cm^{-3} are obtained from the ratios of losses to the absorption cross-section. 40

3.1 Electric field intensity profile example for waveguide structure with 100 nm thick SiO2 gap between Si_3N_4 and Al_2O_3 layers. Buried Si_3N_4 is 4 μm wide and 100 nm thick, and the blanked deposited Al_2O_3 is 2 μm thick. 44

3.2 Electric field intensity profiles with Al_2O_3 refractive index of 1.65 for (a) 980 nm fundamental TE pump mode, and (b) 1550 nm fundamental TE signal mode. Excellent pump and signal mode overlap: $\Gamma_{overlap} = 0.9897$ 45

3.3 Electric field intensity profiles with lower Al_2O_3 refractive index of (a) 1.60 for 980 nm fundamental TE pump mode, and (b) 1.58 for 1550 nm fundamental TE signal mode. Pump and signal mode overlap is also slightly decreased: $\Gamma_{overlap} = 0.9699$ 46

3.4 Electric field intensity profiles with lower Al_2O_3 refractive index of (a) 1.60 for 980 nm fundamental TM pump mode, and (b) 1.58 for 1550 nm fundamental TM signal mode. Again, excellent pump and signal mode overlap: $\Gamma_{overlap} = 0.9868$ 46

3.5 Spectral response of example Bragg gratings with maximum reflectances at around 1550 nm. Responses for (a) reference, (b) reduced coupling strength, and (c) reduced coupling strength but increased coupling length 50

3.6 (a) Top-down schematic diagram, and (b) reflectivity as a function of perturbation magnitude for 4 μm wide 100 nm thick Si_3N_4 waveguide with a 100 nm SiO_2 spacing on top, as shown in Figure 3.1. 50

3.7 Cross-sectional view of die where dicing saw easily clears the edges of the RIE-etched trenches. Coupling light in and out of on-chip devices is much easier using the smooth facets. 52

3.8 Schematic diagram of laser measurement setup using double sided, polarization controlled 980 nm pumps, and spectrum analyzer for characterization. Laser output is measured from the left side of the on-chip device, where the partially reflecting grating is placed. 53

3.9 Spectral distribution of on-chip power displaying lasing at 1533.4 nm wavelength with 3.9 μW output power and over 38.9 dB side-mode suppression ratio. Laser cavity was pumped by TM polarized 980 nm light from both sides with a total power of 1.6 W. 53

3.10 Common scale intensity plots of minor electric field components for different polarizations: (a) E_y for TE mode, and (b) E_x for TM mode. 55

LIST OF TABLES

2.1 Summary of deposition parameters and resulting characteristics of optically low-loss Al_2O_3 films deposited with the Lab 18 sputter tool 36

CHAPTER 1

MOTIVATION FOR SILICON PHOTONICS

1.1 Why Integrate Optics With CMOS Technology?

After its invention in 1948 [1], the transistor has quickly become a vital component in electronic devices, and is considered by many as one of the greatest inventions of the 20th century [2]. With the developments in the complementary metal oxide semiconductor (CMOS) technology [3-5], transistor dimensions have decreased from the micrometer scale nodes of the 1980s to the 22 nm standard of 2012, as shown in Figure 1.1. With increased integration density, transistor-based electronics have become scalable and affordable, and enabled most of the technology we take for granted today such as mobile phones, tablets, computers, and televisions. International Technology Roadmap for Semiconductors 2012 Report [6] predicts the scaling trend to continue towards a 5 nm node by 2020.

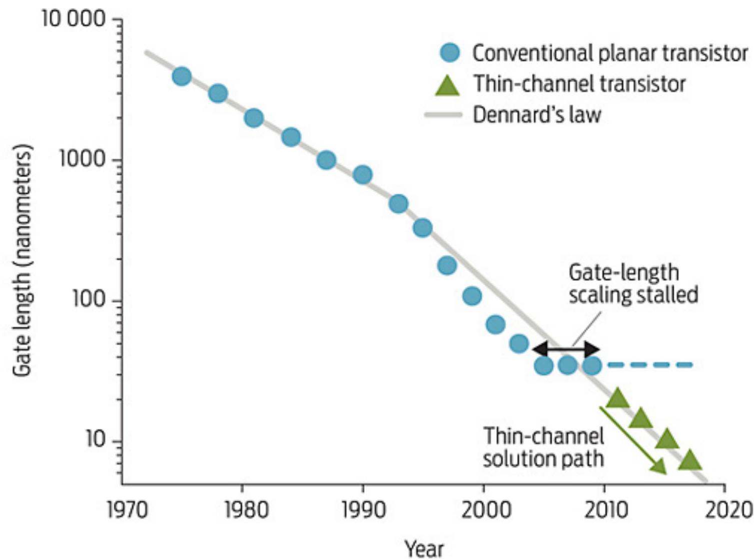

Figure 1.1 – Scaling trends for transistor gate length (known as Dennard's Law) from 1970 to the projected node sizes of 2020 [7]

In conjunction with the smaller node sizes in transistors, the electronic industry has also seen dramatic increases in the clock frequency of transistor-based devices such as microprocessors. Increasing clock speeds basically amounts to a greater number of floating-point operations per second (FLOPS), and therefore faster completion of a given set of instructions. However, around 2003, the increase in clock speeds experienced a sharp turn [8] and has since settled around 3-4 GHz as in Figure 1.2. Most of the frequency increase between 1985 and 2000 has been a result of faster and

parallel implementations of basic circuitry components and widespread use of pipelining techniques [9]. However, with increasing clock speeds the amount of power used and heat generated by microprocessors have also increased dramatically. The power consumption had reached such a point that further increases in clock speed could not be tolerated any more, and cooling the microprocessors required more energy than operating them. The power consumption issue fueled the development of multi-core processors which contain comprised of more than one independent CPUs [10]. With properly designed software, multi-core processors can simultaneously execute multiple sets of instructions, decreasing the overall computation time.

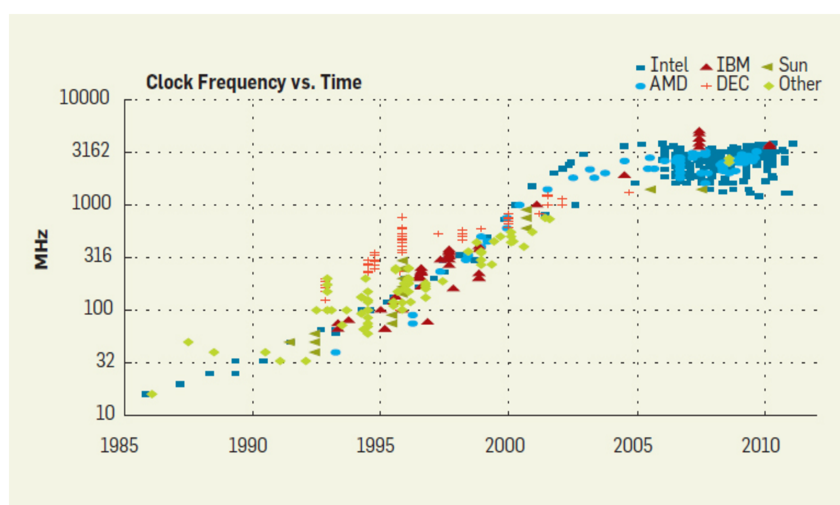

Figure 1.2 – Scaling trends for processor clock frequency from numerous manufacturers since 1985 [9]. Clock frequency clearly levels off around 3-4 GHz after 2003.

Most computation devices we use today are equipped with multi-core processors for their increased efficiency over their single-core counterparts. However, unlike what one might expect, running two separate programs or a two-threaded program on two separate cores usually does not yield twice the performance. This is due to the additional cycles required for the individual cores to communicate with each other and various memory blocks [8]. This communication latency therefore slows down the overall processor speed. Increasing the internal cache memory sizes in each core can help reduce this latency. However, on-chip cache memory is mostly limited by its physical size, and also is more costly than DRAM or flash memory [11].

In addition to increased communication bandwidth requirements for microprocessors, the increase in computation efficiency also requires improved network bandwidth for off-chip communications. This requirement of

bandwidth increase indicates a growing need for efficient transmission of large pieces of data across multiple servers. For robust connectivity, low noise communication channels are needed in order to ensure low bit-error-rate (BER). Additionally, just like on-chip requirements discussed above, keeping power consumption to tolerable levels is essential for off-chip interconnects. Three dimensional (3D) integration schemes such as the ball-grid array [12] and the through-silicon-via method [13] have been proposed as potential solutions to the off-chip communication bottleneck. Both methods are designed to use the chip surface rather than the perimeter, increasing the number of possible connections. However, they still suffer from inherent limitations of electrical interconnects such as non-uniform current density at high frequencies (also known as Skin effect) [14], long rise and fall times for signal voltage [15], power consumption and cooling requirements, and switching noise [16].

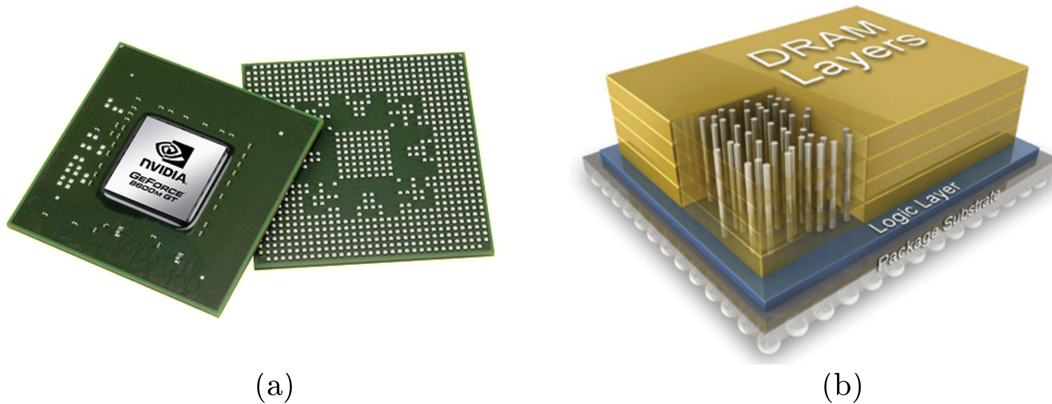

Figure 1.3 – 3D integration schemes for addressing the communication bottleneck: (a) GPU chip with ball-grid array [17], (b) logic and memory integration using through-silicon-vias (concept) [18]

Before the 1970s, data was routinely communicated over electrical wires or by using some form of free space communication in the microwave and radio frequency bands. The prevalence of electrical communication can be attributed to the fact that optical communication platforms need a proper light source and low-loss channels in order to efficiently carry information. Some consider that light would have been a more natural communication medium, since it didn't have to be "invented" unlike electricity [19]. In fact, the first known use of optics dates all the way back to ancient Egyptians and Mesopotamians when they used crystalline rocks as lenses for concentrating sunlight [20]. Throughout its more than two millennia long history, the field of optics has seen immense development and became one of the most well understood and widely used fields in modern science and society. This

progress, especially in its earlier stages, is attributed by many to mankind's efforts of understanding the nature of vision, one of the most important senses we possess [21].

The invention of the laser in the late 1950s [22, 23] and the developments in low-loss optical fibers in the late 1960s [24, 25] stirred most of the initial interest in the field of optical communications. One of the biggest leaps in the field since then was the invention of the semiconductor vertical cavity surface emitting laser (VCSEL) in 1991 [26]. Today, VCSELs are widely utilized in optical communication systems since they can affordably be manufactured in bulk. However, by inherent limitations of the vertical laser cavity design, each VCSEL requires its own optical fiber to communicate with a given node. This is why electrical and VCSEL based interconnects are similar from an integration perspective, since their large-system scalability is not feasible. In contrast, systems where multiple data channels are multiplexed onto the same channel can provide much larger bandwidths within much smaller footprints. An example of such a system is a wavelength division multiplexed (WDM) communication network where a number of optical carrier signals are combined into one fiber by using different wavelengths. A schematic illustration of such a WDM system is shown in Figure 1.4.

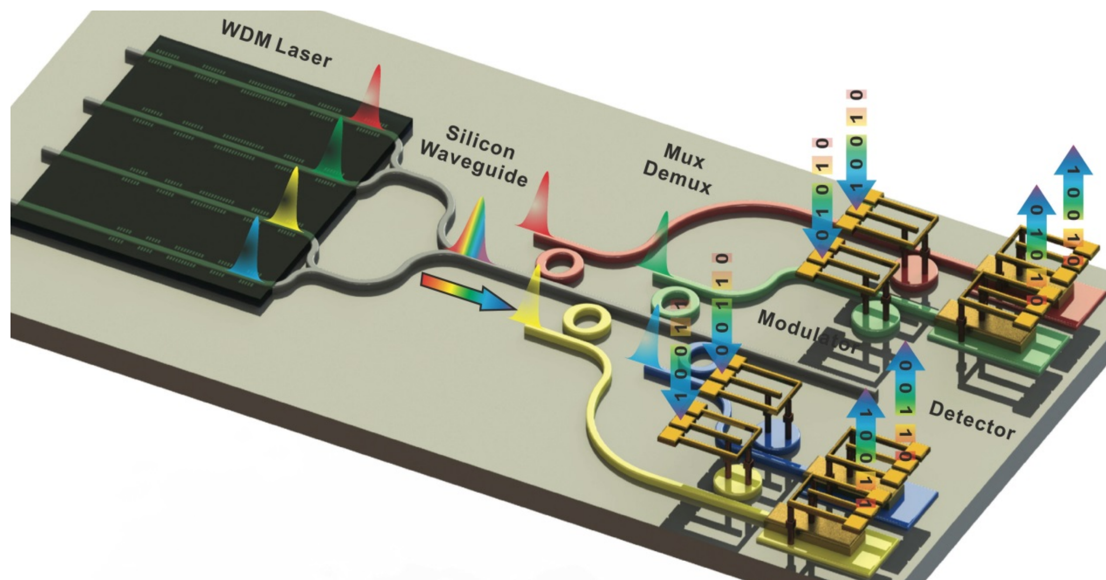

Figure 1.4 – Schematic diagram of on-chip silicon photonics link featuring wavelength division multiplexed laser array, multiplexers, demultiplexers, modulators, and detectors. [27]

The affordability and scalability of chip-sized interconnect systems depend on if they can be manufactured using the existing multi-billion dollar electronics fabrication infrastructure. This fabrication compatibility is one of the main goals of silicon photonics, where silicon and other CMOS compatible materials are used as optical media for altering and guiding light. Over the past few decades, the field of silicon photonics has seen tremendous progress; and many on-chip optical devices including modulators, multiplexers, waveguides, and detectors have already been demonstrated. Examples are shown in Figure 1.5.

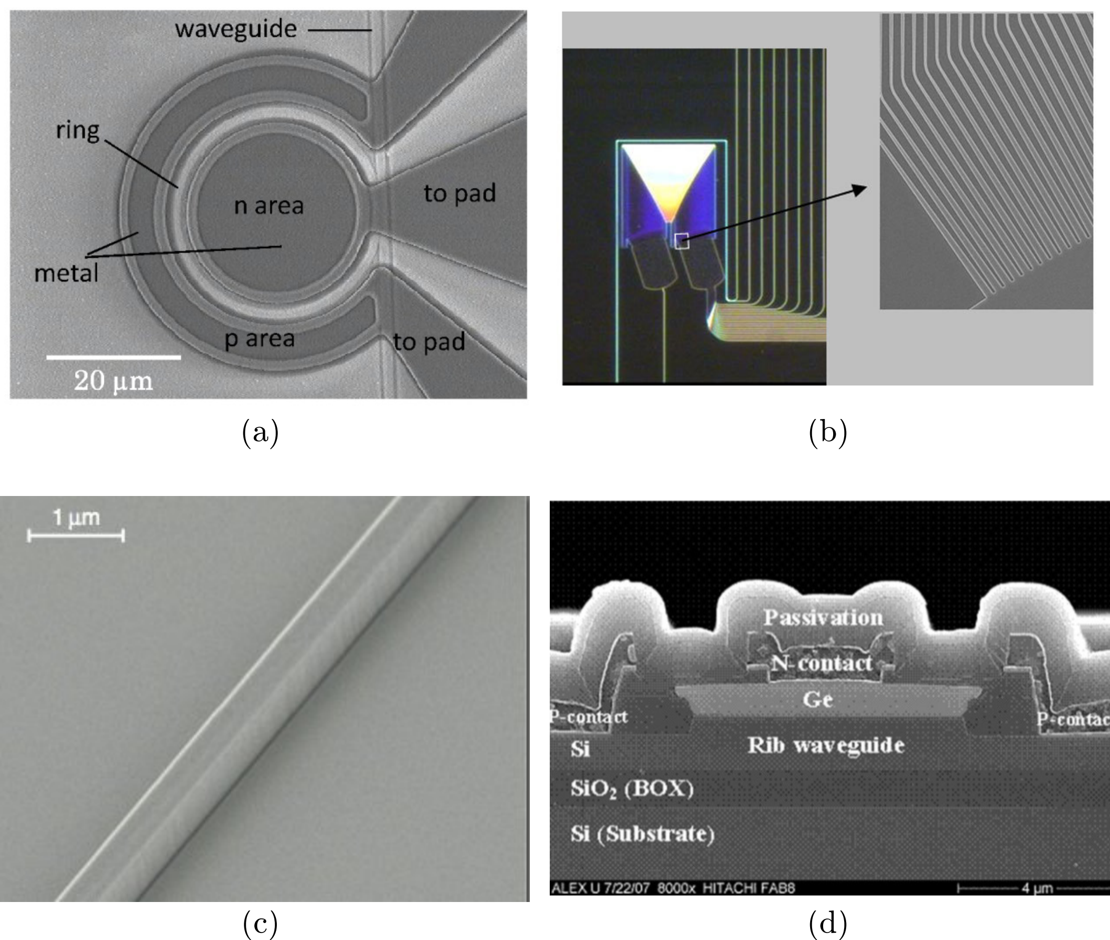

Figure 1.5 – Collection of passive optical devices on-chip: (a) modulator [28], (b) multiplexer [29], (c) waveguide [30], (d) detector [31].

Optically active op-chip silicon-based devices, those that can generate light, are not as easy to demonstrate as passive devices that only change various properties of an incoming light beam. This is due to silicon's indirect bandgap energy, which makes light emission in silicon an extremely inefficient process. Silicon-based active optical devices such as amplifiers and lasers therefore

remain as missing components of a CMOS compatible optical interconnect. Possible substitute materials and other "on-silicon" lasing mechanisms are discussed in the next section.

1.2 Integrated Lasers Solutions

The inability of silicon to efficiently generate light led researchers to seek other means of light emission in silicon-based platforms. Among the most well-known on-silicon light sources are III-V hybrid integrated lasers, strained germanium-on-silicon lasers, silicon Raman lasers, and rare-earth doped amorphous glass lasers. Given below is a brief explanation of each laser type with advantages and disadvantages.

- **III-V Hybrid Integrated Laser:** This type of laser is made from a combination of silicon and III-V compound semiconductors like InP or GaAs. Due to their direct bandgap, these III-V semiconductors are much more efficient in light emission than silicon. The main goal of hybrid integration is to combine these efficient light emission processes in III-V semiconductors with the low-cost integration solutions that silicon fabrication technology offers [32]. Specifically, by wafer bonding an AlGaInAs epitaxial structure to patterned SOI wafer, electrical pumping can be utilized while guiding the light in the SOI layer [33]. However, fabrication complexity is increased due to the epitaxially grown layers of compound semiconductors. Also, depending on the specifics of the design, micrometer precision alignment may be necessary for efficient coupling of light from the lasers to the silicon waveguides [34].

- **Strained Germanium-on-Silicon Laser:** The crystal structure of a material plays an important role in determining the band structure of that material. Under stress, the crystal structure is displaced from its relaxed state, inducing changes in the bandgap energy and various electronic transitions. In one such example, germanium was grown epitaxially on silicon, and then thermally stressed in order to shrink its direct bandgap energy [35]. As a result, direct gap light emission was enhanced, and a room-temperature edge-emitting laser was realized by optical pumping [36]. Like the III-V hybrid lasers, strained Ge-on-Si lasers also require lengthy fabrication steps, and are therefore more difficult to implement in a cost-effective and scalable way.

- **Silicon Raman Laser:** In contrast to most other types of lasers where light is generated by stimulated emission, in Raman lasers, light is emitted as a result of Raman scattering. Raman lasers are optically pumped; and absorbed photons are re-emitted with a fixed, material dependent Stokes shift. One main advantage of Raman lasers is that they can generate light in wavelength regions that may otherwise be inaccessible by means of stimulated emission [37]. Moreover, a wide range of Raman crystals are available for frequency conversion. However, depending on the type of crystal used, thermal loading issues may be experiences at high pump powers [38].

- **Rare-Earth Doped Glass Lasers:** This alternative solution for realizing an on-chip light source is derived from long-distance optical communication networks. Due to their ease of fabrication using CMOS compatible methods, and emission bands suitable for fiber-optics communications, Er^{3+} doped oxides have been widely studied [39-41]. In the 1990s, Er^{3+} doped fiber amplifiers became one of the biggest driving forces behind the bloom of the internet with the invention of the erbium-doped fiber amplifier (EDFA) [42, 43]. In rare-earth doped media, the atomic energy levels of rare-earth ions are used in the stimulated emission process. With their easily deposited and CMOS-compatible host glasses, lasers based on rare-earth electronic transmission possess great potential as scalable solutions to the on-silicon laser problem. One possible issue with use of glasses as the guiding dielectric is due to their low refractive indices. With glass waveguides, reduced index contrast can yield devices that are sensitive to refractive index changes due to fabrication differences.

1.3 Erbium-Doped Amorphous Aluminum Oxide ($Er^{3+}:Al_2O_3$)

Of all 15 lanthanides (those with atomic numbers 51 through 71), erbium is one of the most commonly used dopants. This has to do with the characteristics of silica fibers which have become standards over which optical signals are carried over long distances like the Atlantic Ocean. Figure 1.6 shows optical losses of silica fiber per unit length as a function of wavelength. For shorter wavelengths closer to the visible spectrum, absorption losses are dominated by Rayleigh scattering. For wavelengths longer than 1.7 μm, infrared absorption losses are the dominant factor in determining the fiber losses. This leaves a minimum loss window around the wavelength of 1.55 μm

that is suitable for long distance communications with the use of minimum optical power.

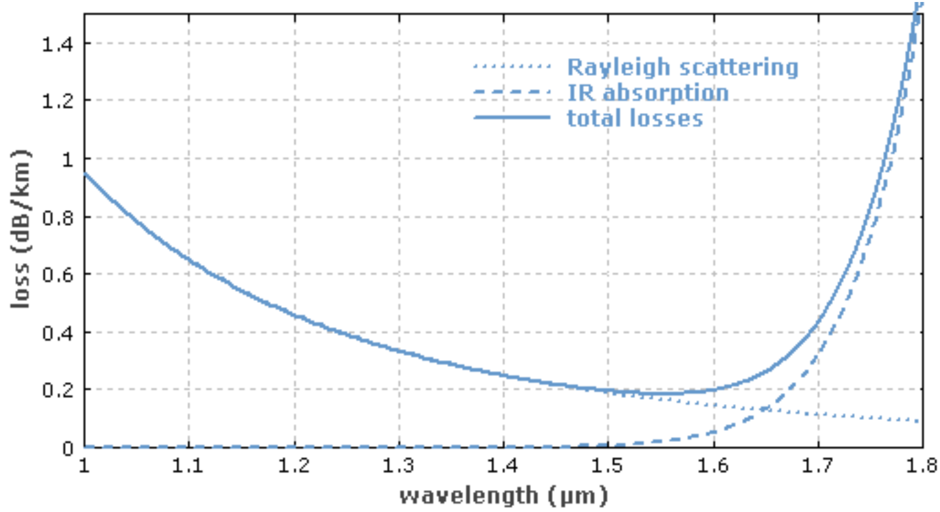

Figure 1.6 – Optical losses per unit length of silica fiber. Influences by Rayleigh scattering at shorter wavelengths, and infrared vibrational losses are clearly observed. Absorption peaks of OH^- ions are not shown, as they can be eliminated under proper deposition conditions [44].

It turns out that, due to the number of electrons in its ionic state, erbium allows for transitions at wavelengths of 0.55 µm, 0.98 µm, 1.45 µm, 1.55 µm, and 2.90 µm, as shown in Figure 1.7. The 1.55 µm emission arising from the $^4I_{13/2} \rightarrow {}^4I_{15/2}$ transition is of particular interest as it directly coincides with the low-loss window of silica fibers, and also since it has a lifetime of approximately 10 ms. Due to the long lifetime of the upper lasing state, it is much easier to achieve population inversion in comparison to semiconductor gain media which typically have lifetimes of a few nanoseconds. The emission spectrum of erbium ion Er^{3+} also provides possible pumping windows around 0.98 µm and 1.45 µm, making Er^{3+} an excellent candidate for optically pumped on-chip light emission devices.

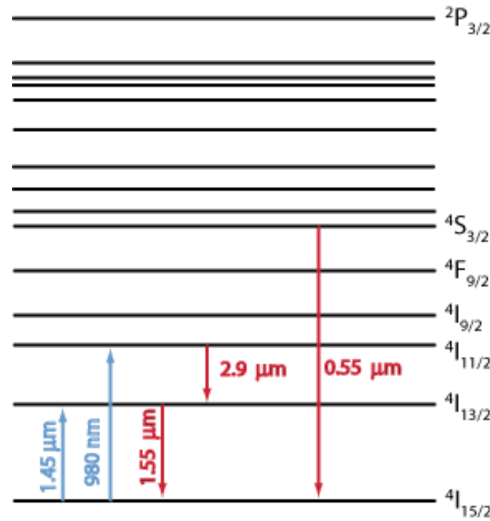

Figure 1.7 – Energy diagram and commonly used transitions of erbium ion Er^{3+} [44]

Despite all these advantages of using an Er^{3+} based system, achieving gain or lasing output from Er^{3+} doped media can still be challenging. One of the main challenges encountered stems from the relatively small absorption cross section of Er^{3+}, as shown in Figure 1.8. Concentrations upwards of $1x10^{20}$ cm^{-3} are routinely needed in order to achieve sufficient absorption [45]. Increased concentration however results in luminescence quenching effects where lifetimes of ions and the output intensity are significantly reduced [46]. Various co-doping methods using ytterbium (Yb^{3+}) have been shown to reduce quenching effects [47], but are not pursued in this thesis.

In order to use Er^{3+} or any other rare earth dopants in silicon photonics applications, suitable host media need to be found. Among general requirements like CMOS-compatibility, ease of material processing, and minimal propagation losses, requirements specific to the dopants such as good Er3+ solubility, and low phonon energy to reduce non-radiative decay are desired. Common crystalline hosts such as LiNbO3 (lithium niobate) or Y3Al5O12 (yttrium aluminum garnet or YAG) are suitable for Er3+, but require epitaxial growth. Silicon has extremely low Er3+ solubility, and is therefore also not suitable. Any polymers like PMMA are thermally unstable, and also CMOS-incompatible. This leaves amorphous glasses like silica, phosphate, fluoride, and alumina as possible hosts that can provide the broad gain spectrum needed for WDM architecture, and be deposited using CMOS-compatible equipment relatively easily. One issue that has been mentioned in the previous section is the low index contrast provided by the glass guiding media. Of the types listed, alumina is reported with the highest refractive indices around 1.65, whereas the others have remained around 1.4-1.5 [48-50].

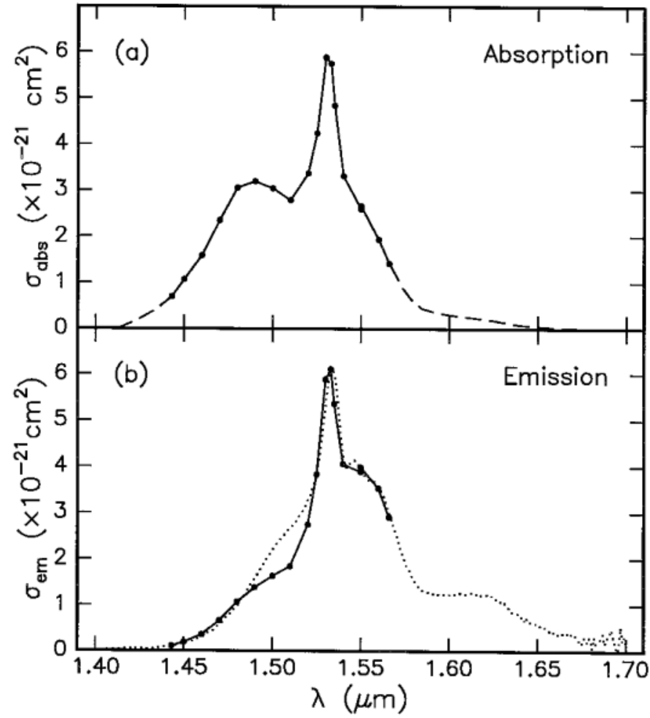

Figure 1.8 – (a) Absorption and (b) Emission cross-section spectra of Er^{3+} between 1.4 μm and 1.7 μm [51]

The remainder of this thesis explores a deposition procedure of Er^{3+}:Al_2O_3, and demonstrates CMOS-compatible laser operation using the process recipes developed. Chapter 2 focuses on development of the deposition process, how various process parameters affect the optical quality of the deposited Al2O3 and Er^{3+}:Al_2O_3, and the metrology of film properties important for active device operation such as dopant concentration. Chapter 3 discusses the design methodology of creating a process flow suitable for the deposition explained in Chapter 2. Details of the laser cavity, including pump and signal mode solutions, and experimental demonstration of lasing results are also presented in Chapter 3. In Chapter 4, materials and devices results are summarized, and a vision for Er^{3+}:Al_2O_3 based devices is given with examples of possible future work.

CHAPTER 2

FABRICATION METHODOLOGY AND MATERIAL CHARACTERIZATION

2.1 Advantages of Sputtering

Sputtering is a widely used physical vapor deposition (PVD) process for fabrication of thin films [52]. Due to its relative simplicity, sputtering can reliably and consistently yield the host media required for integrated optics. First of all, sputtering allows for a practically contaminant free deposition in an ultra-high vacuum environment. In contrast, deposition techniques such as CVD or sol-gel based methods inevitably introduce OH^- contamination, reducing luminescence intensity in active devices [53]. Secondly, one can use reactive sputtering to deposit films of thicknesses on the order of micrometers in only a few hours. Comparable methods such as atomic layer deposition (ALD) or other epitaxial growth techniques, although can produce films of excellent quality, suffer from their slow deposition rates. Therefore methods such as ALD and epitaxial growth are commonly used for applications where film thicknesses are on the order of tens of nanometers [54]. Additionally, sputtering allows for deposition on a variety of substrate sizes. This makes it possible to easily transfer the process from centimeter sized dies used for prototyping to larger substrates such as the commonly used 300 mm and 200 mm wafers.

In silicon photonics, the fabrication methods need to not only be able to reliably produce the desired films, but also be CMOS compatible. For integration with electronics, and in order for making use of the already existing multi-billion dollar silicon manufacturing technology, the fabrication techniques used for integrated photonics must satisfy the requirements of the CMOS industry. This compatibility ensures the quality of photonic integration as well as providing the photonic devices access to control circuitry for electronic signal generation and processing protocols [55]. The ultra-high vacuum environment used in sputtering eliminates any contaminants such as gold, which greatly inhibits electronic device performance. The parameter space for sputter deposition also allows for high quality films to be produced at temperatures lower than 525 °C, over which CMOS structures have been shown to deteriorate [56].

2.2 The Kurt J. Lesker Lab 18 Sputtering Tool

In order to be able to investigate co-doping possibilities, and for the quality of the sputtered films, a new sputtering tool was purchased. Made by Kurt J. Lesker Company (KJLC), Lab 18 is a modular thin film deposition system that can be configured to be used for sputtering, electron beam deposition, or thermal evaporation. A Lab 18 system was purchased, customized for ultra-

high vacuum sputtering, and installed in MIT's NanoPrecision Deposition Laboratory, as shown in Figure 2.1.

Figure 2.1 – Kurt J. Lesker Lab 18 sputtering system located in NanoPrecision Deposition Laboratory at MIT

Summarized below are some of the significant advantages of the Lab 18 system in comparison with other similar systems.

- **Loadlock:** In systems where the process chamber has to be vented for a new wafer to be loaded, the user has to wait for the chamber to pump down to an acceptable base pressure. Sometimes, in such systems, reaching a base pressure of 10^{-6} Torr can take as long as a few hours. The Lab 18 system is equipped with a loadlock, which is a secondary vacuum chamber used for transferring substrates into the main process chamber. As the loadlock is much smaller, it can be pumped down much quicker (in about 10 minutes), and therefore allows for quicker operation of the system. More importantly, any deposition process can be carried out without compromising the integrity of the process chamber vacuum. This in turn results in higher quality films free of any possible contaminants.

- **Radio Frequency (RF) power supplies:** Conventional sputtering systems use direct current (DC) power supplies, which work with metallic targets. However, for dielectric targets or reactive deposition, plasma arcing becomes one of the most important challenges. Lab 18 uses RF power supplies to prevent excessive charge-up of dielectric

layers to reduce the risk of plasma arcing. Lab 18 is equipped with four RF power supplies. One of these is dedicated to the substrate, which is used for creating a substrate bias before or during deposition for purposes of substrate cleaning, etchback, or smoothing the surface of the deposited film. This power supply is rated at 100 W of output power. Of the three remaining power supplies two of them are paired with dedicated sputtering guns. These are usually used for dopants metals such as Er and Yb. Having dedicated power supplies for each dopant allows for co-doping, which has been shown to enhance active device performance [57]. The remaining power supply is usually used for the metal target whose oxide is being deposited. In this manner, the power consumption is also minimized for producing stack-like structures where alternating layers of oxides are deposited. These three remaining power supplies are rated at 600 W.

- **Downward facing substrate:** The direction that the substrate faces directly affects the quality of the deposited films. In systems where the substrate faces upwards, flakes and other contaminants are brought down onto the substrate surface by gravity, and can be trapped in the deposited film. On the other hand, these systems usually allow for less complicated wafer loading mechanisms, and use of samples with smaller and varying sizes, as they don't have to rest on a carrying platform. In Lab 18, the substrate faces downwards. This prevents flakes from sticking onto the surface by gravity. However, deposition on differently sized wafers or dies requires specially made substrate holders.

- **Ion beam:** In addition to a substrate dedicated power supply, this Lab 18 system is also equipped with an ion source directed at the substrate. This allows for ion-assisted deposition, where any sputtered material that is poorly adhered to the substrate is knocked off. It is anticipated that controllable ion bombardment of the substrate would yield smoother and denser films [58].

2.3 Sputtering Process Optimization for Low-Loss Al_2O_3 and Uniformly Doped Er^{3+}:Al_2O_3

In any deposition system, the film quality vastly depends on process parameters including the process pressure, gas flows and ratios, power delivered to targets, substrate temperature, and the distance between the targets and the substrate (the throw distance). Optimization for high-rate and high-quality deposition in this multi-dimensional space can be extremely difficult and time consuming. However, it may be possible to isolate some or all of these parameters by considering what quantities actually affect the physics of the deposition process.

2.3.1 Standard Operating Procedure for Lab 18

Regardless of how well optimized the deposition parameters are, the general usage and the cleanliness of substrates placed inside the vacuum chamber also greatly affects the process success and consistency. Therefore, any parameter optimization must be conducted under a standard operating procedure. This involves not only certain requirements on some of the steps of fabrication, but also aspects of tool use outside of fabrication like consistent recordkeeping. To this end, the following requirements are imposed for the use of this sputtering tool.

- Each wafer is assigned an ID in the form of K###, and a corresponding record is created in a paper log, an independent log on a separate computer.

- For each substrate and for each process, a separate recipe is created with the same name format as above. During the process, the record function is used on the controller software to track system parameters. These trend files stored in the Lab 18 computer.

- Wafers and dies are loaded with a pair of machine-dedicated tweezers onto the wafer platen inside the loadlock.

- The loadlock is pumped down to $6x10^{-5}$ Torr before transfer into the process chamber is initiated. This is determined by how fast the loadlock can be pumped down from atmospheric pressure, and how much the process chamber pressure is affected by opening the isolation valve of the loadlock.

- The substrate heater is ramped up to 400 °C at a rate of 10°C per minute, and held there for two hours under rotation. This outgassing step is introduced in order to ensure cleanliness of the substrate and the chamber from any contaminant gases. The 400 °C limit is imposed by the thermal limits of CMOS structural integrity and a safety factor of roughly 100 °C. The rate and rotation are included for achieving the most uniform temperature distribution across the substrate surface. Lastly, the duration of outgas is determined by how much the partial pressures of H_2, He, N_2, H_2O, O_2, Ar, and CO_2 change during this outgas. As shown by the residual gas analyzer scan in Figure 2.2, after an outgas of two hours, the partial pressures of these gases have decreased to a level that is similar to what they were before the substrate had been loaded in.

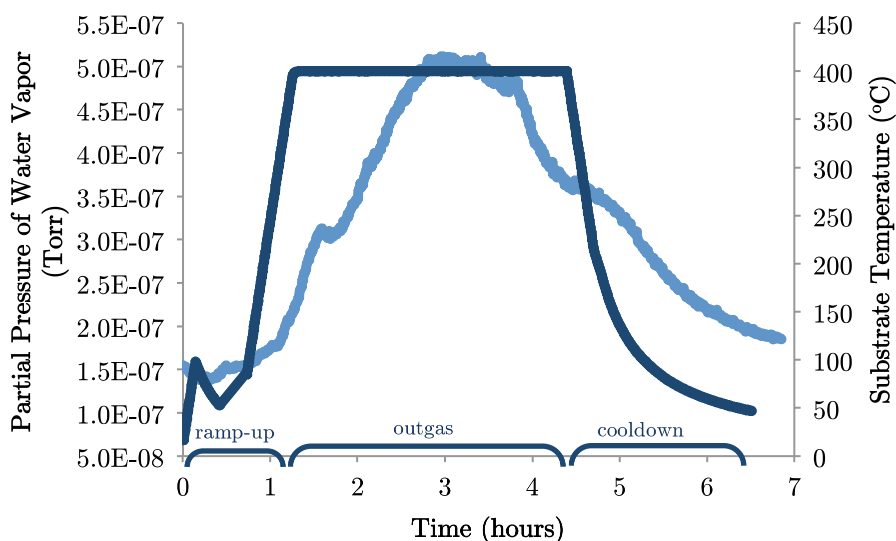

Figure 2.2 – Water vapor partial pressure inside the process chamber (light blue), and substrate temperature (dark blue) during outgas. After the substrate temperature is held at 400 °C for two hours, water pressure has dropped to levels similar to what it was before the outgas.

- At any point during the process, if the substrate temperature needs to be changed, the heater is ramped up or down to the desired value at a rate of 10°C per minute. This ensures uniform temperature distribution during the whole process.

- After plasma has been initiated, all targets that are going to be used in this deposition process are sputtered at 400 W for 5 minutes for

cleaning and uniformity of the deposited film. This is called pre-sputtering, and is a common practice in similar sputtering and evaporation like PVD methods [59]. The reason for choosing 400 W will be explained in Section 2.3.2.

2.3.2 Determining the Optimum Deposition Conditions for Low-Loss Al_2O_3

In reactive sputtering, the oxidization of the target material is a well-documented and experimentally verified phenomenon [60-62]. It is also one of the most important mechanisms by which the quality of the resultant material and the rate of deposition are determined. Therefore, it makes sense to investigate this oxidization behavior in order to gain insight into how this specific sputtering tool responds to changing reactive gas flow in its current configuration. This can be done in the following manner.

By sputtering mechanics, we know that delivering a greater amount of power to a target material creates a greater magnitude of bias voltage across it. This attracts more Ar^+ ions, increasing the number of atoms knocked off the surface of the target and sputtered onto the chamber surfaces. Consequently, and as experimentally shown [63], this results in a higher deposition rate. In many applications, for utility, consistency, and the repeatability of the process, a reasonably high, yet constant deposition rate is required. The maximum amount of power available in the Lab 18 sputter tool for the Al target is 600 W. However, in order to make best use of the generator lifetime, this power supply is operated at a maximum of 400 W. This is the first parameter that is chosen for optimization of the low optical loss Al_2O_3 deposition process. For ease of operation, targets are also pre-sputtered at 400 W.

Once a radio frequency output power has been determined, the oxidization behavior can be modeled. The goal of this step is to determine the operating state of the target as a function of reactive gas flow, and use this information to identify a parameter subspace for obtaining the correct stoichiometry of Al_2O_3 while maintaining the highest deposition rate possible. The operating state of the target can be metallic or oxidized (also known as poisoned), and is identified by the discharge voltage developed across the target. After the O_2 flow has been increased sufficiently high to cause an abrupt drop in this discharge voltage, the target surface is known to be poisoned [64]. Measurements shown in Figure 2.3 clearly demonstrate this expected behavior of metallic to oxidized target transition with increased reactive gas flow.

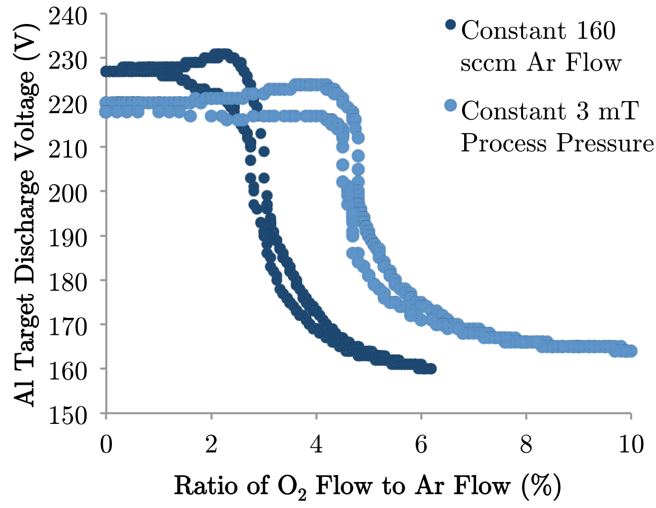

(a)

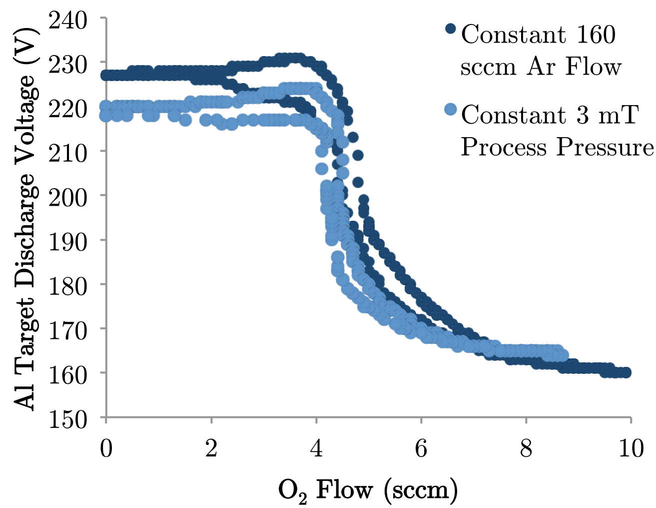

(b)

Figure 2.3 – Discharge voltage developed across the Al target as a function of (a) the ratio of O_2 flow to Ar flow, and (b) O_2 flow. Dark blue indicates measurements under constant Ar flow of 160 sccm, whereas light blue is used to display discharge voltage measured at a constant pressure of 3 mT. Both sets of measurements are taken with maximum pumping speed possible.

Under both constant Ar flow and constant process pressure conditions, the abrupt drop in the discharge voltage is observed at an O_2 flow of 4.0 sccm. This also marks the stoichiometric point for Al_2O_3. In other words, using a smaller amount of O_2 flow results in metallic films, whereas higher flows fully poison the Al target and significantly reduce the deposition rate [65]. Figure 2.3 also shows the well-known hysteresis effect where changing the reactive gas flow can result in the discharge voltage to increase or decrease depending on the current state of the target (metallic or oxidized). As a result, for a given gas flow, the target can be in the metallic or oxidized state, depending on the history of the gas flow. Therefore, a small increase in the reactive gas flow can lead to a dramatic decrease in the discharge voltage. A following decrease of similar amount in the reactive gas flow however does not bring the system back into the same stoichiometric operating state, due to the hysteresis shown. This makes it difficult to operate the system at this stoichiometric point. However, it has been shown that increased Ar flow rates can make the hysteresis loop shrink, and eventually collapse to a single curve at high enough pumping speeds [66, 67]. This is why the system is operated at the maximum pumping rate possible with a turbomolecular pump where the gate valve is left in the fully open position. On the other hand, it is also known that increased deposition pressure, which inherently results from increased Ar flow rate at constant pumping speed, causes a slower deposition rate due to reduced discharge voltage, and also a lower refractive index [68-70]. This requires experimentation with different process pressures, which can be adjusted by the mass flow controllers (MFCs) at a given pumping speed.

Once the gas flows for different deposition pressures have been determined, the substrate temperature for deposition is considered. The main goal here is to determine an optimum substrate temperature at which optically low-loss Al_2O_3 films can be deposited consistently. In order to characterize the optical loss, a Metricon prism coupler setup is used where the intensity of scattered light is recorded with a fiber. This intensity profile is then fitted with an exponential decay, from which the extinction coefficient is extracted [71].

The deposition temperature is measured by a thermocouple that is placed next to the substrate heater, which the substrate is placed directly underneath. Therefore, temperature distributions of substrates of different materials may vary. This can be monitored by the current delivered to the substrate heater in order to keep the substrate at a certain temperature. As the heater is automatically controlled, current is adjusted in order to stabilize the substrate temperature. This is plotted in Figure 2.4 for temperature ramp-up from room temperature to 400 °C for three different substrate types: an 8" Si wafer, a 6" Si wafer with a holder around it, and two 20 x 25 mm Si dies with appropriate housing placed in the 8" opening.

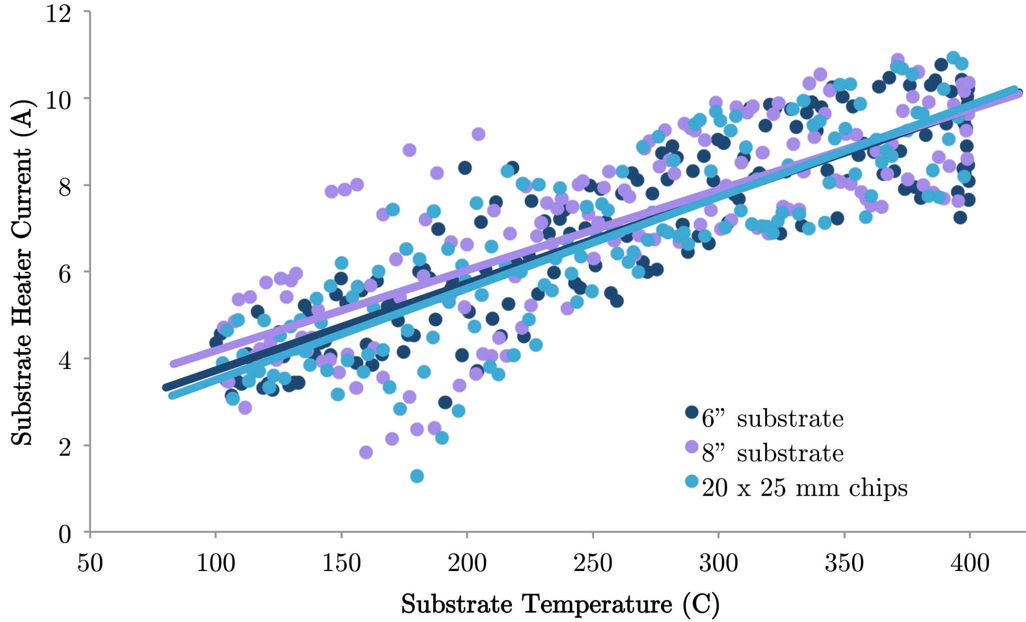

Figure 2.4 – Variation in the current supplied to the substrate heater during ramp-up from room temperature to 400 °C for 6” and 8” substrates, and 20 x 25 mm chips

It is seen that similar amounts of substrate heater current are required to keep different substrate types at given temperatures. We therefore conclude that no extra temperature calibration steps are necessary when the substrate type is changed. A reliable process can then be developed with 6” Si substrates, and be easily transferred to larger 8” Si wafers or smaller dies.

In order to achieve amorphous alumina, the substrate temperature during deposition must be kept relatively low. Crystalline forms have been observed at temperatures as low as 250 °C [72]. Sufficiently low deposition temperature requirement is also imposed by CMOS compatibility as discussed previously. Hence, although Lab 18 can reach substrate temperatures up to 800 °C, optimization is performed for temperatures under 450 °C. As shown below in Figure 2.5, 250 °C was determined to be an appropriate temperature for achieving low-loss Al_2O_3. Optical losses below 0.1 dB/cm were achieved. At lower losses, a longer than 5 cm propagation length is needed in order to observe comfortable measurable decreases in the scattered light intensity.

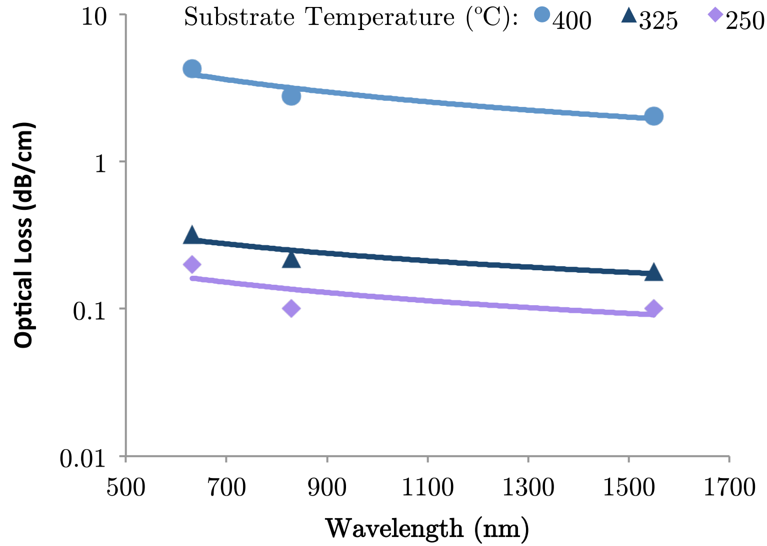

Figure 2.5 – Optical losses of reactively sputtered Al_2O_3 films as a function of substrate temperature during deposition. Other deposition conditions such as pressure, RF power delivered to the substrate and the Al target, and O_2 flow are kept constant at 5 mT, 90 W, 400 W, and 4.1 sccm, respectively.

Another crucial parameter the deposition has to be optimized for is the RF power delivered to the substrate. Previous studies have shown that reactively sputtered films under weaker substrate biases exhibit greater surface roughness [73], and higher optical loss due to increased Rayleigh scattering [74]. Similar results have been obtained with the Lab 18 sputter tool, where optical loss decreased to a minimum of 0.1 dB/cm in the C-band of 1530 – 1565 nm with the use of 90 W substrate bias. Weaker substrate biases of 60 W, 30 W, and operation without substrate bias yielded increasingly high-loss films. Optical losses as high as 23 dB/cm were recorded at 632 nm when no substrate bias was used. With use of 90 W substrate bias, losses in the visible and near-to-mid infrared spectra have been reduced to below 0.2 and 0.1 dB/cm respectively. Results are shown in Figure 2.6.

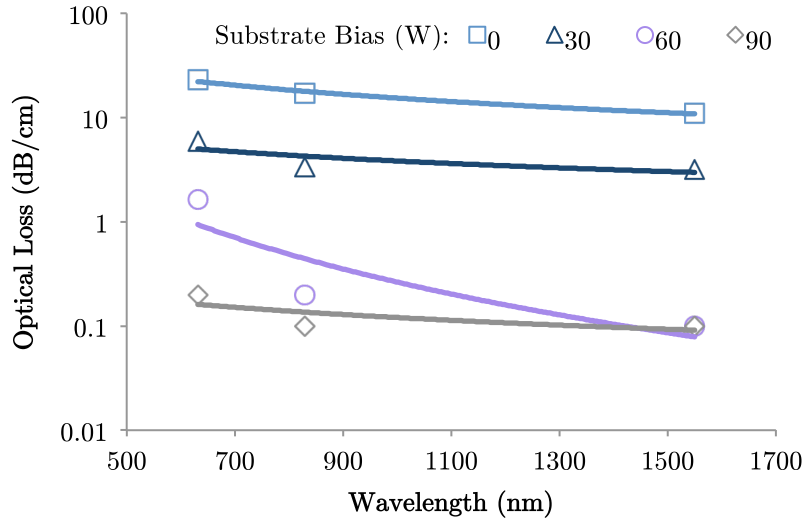

Figure 2.6 – Optical losses of reactively sputtered Al_2O_3 films as a function of substrate bias. Other deposition conditions such as pressure, substrate temperature, RF power delivered to the Al target, and the O_2 flow are kept constant at 5 mT, 250 °C, 400 W, and 4.1 sccm respectively.

As expected, surface roughness of the Al_2O_3 films also decreases with increasing substrate bias. Shown in Figure 2.7 are two atomic force micrographs obtained from films deposited with 90 W of substrate bias and no substrate bias. Significant improvements on surface roughness are observed over a $1\mu m^2$ area. With the use of the substrate bias, root mean squared roughness R_q has decreased by almost an order of magnitude from 3.31 nm to 0.35 nm.

In summary, a region of operation for reliable fabrication of optically low-loss Al_2O_3 has been identified. These process parameters, as well as some of the resulting characteristics of Al_2O_3 are listed in Table 2.1.

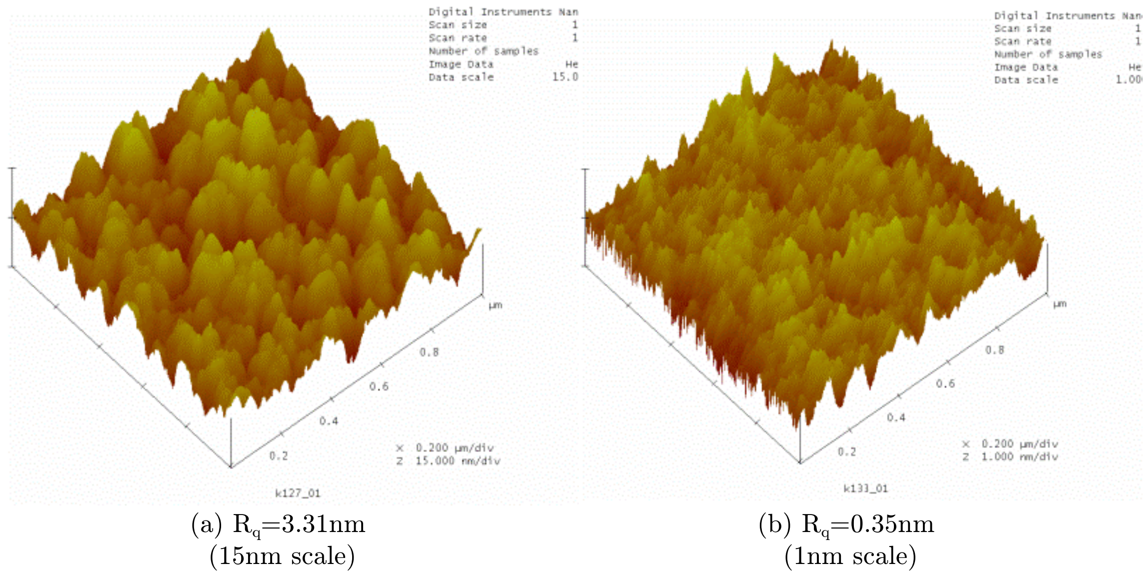

(a) R_q=3.31nm (15nm scale)

(b) R_q=0.35nm (1nm scale)

Figure 2.7 – Atomic force micrographs of films deposited with (a) no substrate bias, (b) 90 W substrate bias over 1µm^2 area. Root mean square surface roughness has significantly decreased, with the addition of 90 W substrate bias. Note the vertical scale differences between the two surfaces, indicating the magnitude of the difference between the surface roughnesses of the two samples.

Substrate Temperature	250 °C
Ar Flow	160 sccm
O_2 Flow	4.0 – 4.3 sccm
Process Pressure	5.0 – 5.1 mT
Al RF Power	400 W
Substrate Bias	90 W
Refractive Index	1.60 @ 632 nm
	1.58 @ 1550 nm
Optical Loss	0.2 dB/cm @ 632 nm
	0.1 dB/cm @ 1550 nm
Surface Roughness	0.35 nm over 1µm^2

Table 2.1 – Summary of deposition parameters and resulting characteristics of optically low-loss Al_2O_3 films deposited with the Lab 18 sputter tool

2.3.3 Characterization of Dopant Concentration

In this section, characterization of Er^{3+} as a rare-earth dopant is considered due to its 1.5 μm atomic transition window. However, a similar procedure can be followed with other possible dopants such as Yb^{3+} or Nd^{3+} to achieve gain or lasing in other bands.

After appropriate process parameters have been identified for low-loss Al_2O_3 deposition, dopant concentration is investigated. The dopant concentration is mainly controlled by the discharge voltage developed across the dopant target metal. Although influenced by the amount of power delivered to the sputtering gun this target is placed in, the discharge voltage is also a function of various other vacuum parameters like the gas flows and process pressure. Nevertheless, the number of atoms sputtered off of a target is determined by the discharge voltage, which dictates the number of Ar^+ ions attracted towards it. Therefore, the analysis of dopant concentration is given as a function of the discharge voltage across the dopant target.

Initial experiments involving Er^{3+} as a dopant have been carried out by simply adjusting the power delivered to the Er^{3+} target. However, upon examination of the trend files, it has been discovered that the discharge voltage changed dramatically during the deposition process. For a constant RF power of 45 W, the discharge voltage developed across the Er^{3+} target has decreased from 59 V to 47 V. When a smaller amount of power was delivered, the discharge voltage changed even more dramatically, as it dropped from 48 V to 15 V for 30 W of RF power. This suggests that films deposited in this manner are likely to exhibit dopant profiles varying with film thickness. In order to mitigate the drift of the discharge voltage, several solutions can be proposed. One possible solution is to actively change gas flows or process pressure during deposition. This change in process parameters during deposition can affect film properties since the Al target is operated just at the edge of being oxidized. Therefore, actively changing process parameters like gas flows or pressure is not advisable. A simpler alternative is to increase the RF power delivered to the Er^{3+} target, so that the discharge voltage stays constant. Some power supplies have DC voltage levelling modes, where power output is controlled automatically to stabilize the discharge voltage. Voltage levelling modes can also be mimicked manually by incrementing the power by 1 W every time the discharge voltage drops by 2 V. By manually incrementing radio frequency power, 60 V and 75 V stable discharge voltages were achieved with RF powers of 45 to 53 W, and 62 to 75 W, respectively. All four cases described here are shown in Figure 2.8. Note that the changes in discharge voltage are not linear in time. This nonlinearity makes it difficult to set constant increase rates in power. Therefore, a power supply that can

automatically control its output to stabilize the plasma discharge is highly desirable.

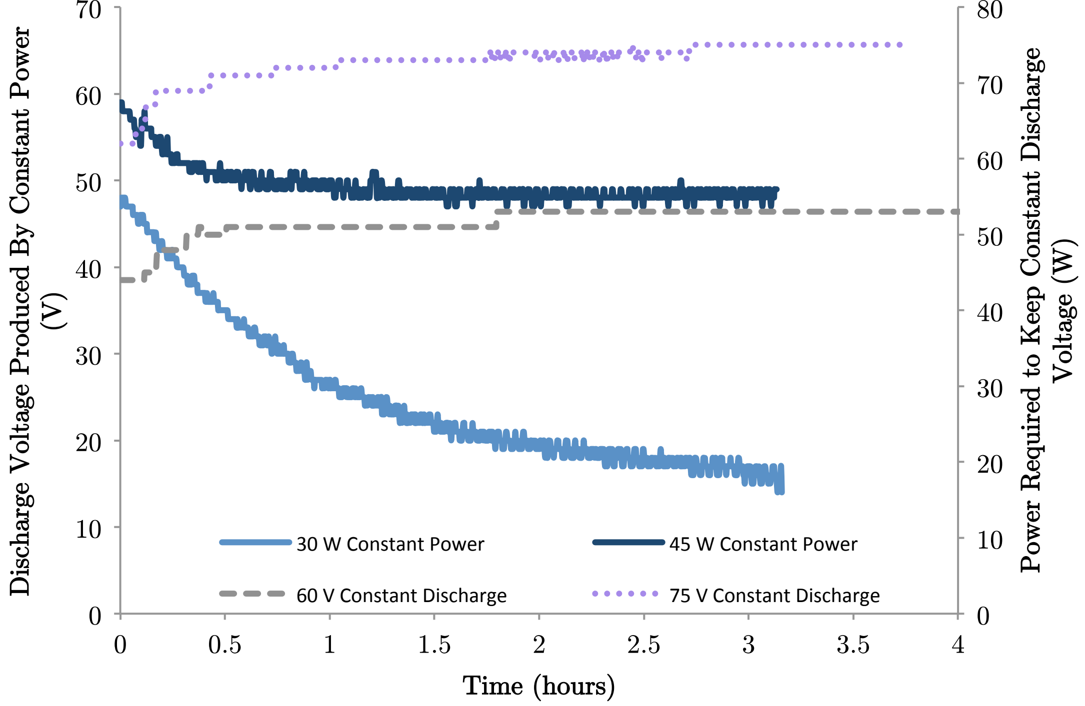

Figure 2.8 – Behavior of erbium discharge voltage under 30 W and 45 W constant RF power (solid lines), and the amount of power required to keep stable erbium discharge voltage of 60 V and 75 V (dotted and dashed lines).

Given a constant discharge voltage, the dopant concentration can then be estimated by the amount of optical loss at a certain wavelength. For this measurement, again, the prism coupler setup is used, along with two external lasers for the bands of interest: 960 – 990 nm for the pump absorption and 1510 – 1580 nm for signal absorption/emission. Along with loss measurements, the absorption cross-section of Er^{3+} is also necessary. The two datasets can then be linked by a dopant concentration, since losses are mainly determined by the concentration for a given absorption cross-section. This is modeled by

$$\alpha(\lambda) = \alpha_{abs}(\lambda) + \alpha_{bcg}(\lambda) = \left(10\log(e)\,\Gamma(\lambda)\right)\sigma_{abs}(\lambda) + \alpha_{bcg}(\lambda) \qquad (2.1)$$

where the total loss $\alpha(\lambda)$ is given in terms absorption and background losses $\alpha_{abs}(\lambda)$ and $\alpha_{bcg}(\lambda)$, and $\alpha_{abs}(\lambda)$ is written in terms of the absorption cross-

section $\sigma_{abs}(\lambda)$, and the mode confinement factor in the core of the waveguide $\Gamma(\lambda)$.

In Figure 2.9, the analysis given in Eq. (2.1) is shown for two films deposited at different Er^{3+} discharge voltages, 60 V and 75 V. As calculated from the losses in the signal band, the first film has an Er^{3+} concentration of 9.5×10^{19} cm^{-3}, whereas the second film has an Er^{3+} concentration of 1.9×10^{20} cm^{-3}. Notice that a 15 V increase in the discharge voltage caused the dopant concentration to double, indicating a non-linear dependence of the sputtered dopant atoms on the discharge voltage. The increase in the dopant concentration is also seen in the increased optical absorption losses for the 980 nm pump band. The excellent overlap of absorption cross-section data with the loss measurements emphasizes low background losses, which are estimated by the last plots as 0.08 dB/cm and 0.29 dB/cm. It is important to note that these are only approximate values, as background losses due to scattering mechanisms are also wavelength dependent. However, these estimates are low enough that they support the loss measurements presented in the previous section. Lastly, with enough dopant concentration, a 20 nm wide bandwidth is obtained where absorption losses are over 3 dB/cm. This confirms that $Er^{3+}:Al_2O_3$ is an appropriate platform for amplifier and laser applications for on-chip routing of wavelength-division-multiplexed signal without any significant cross-talk between spectrally adjacent channels.

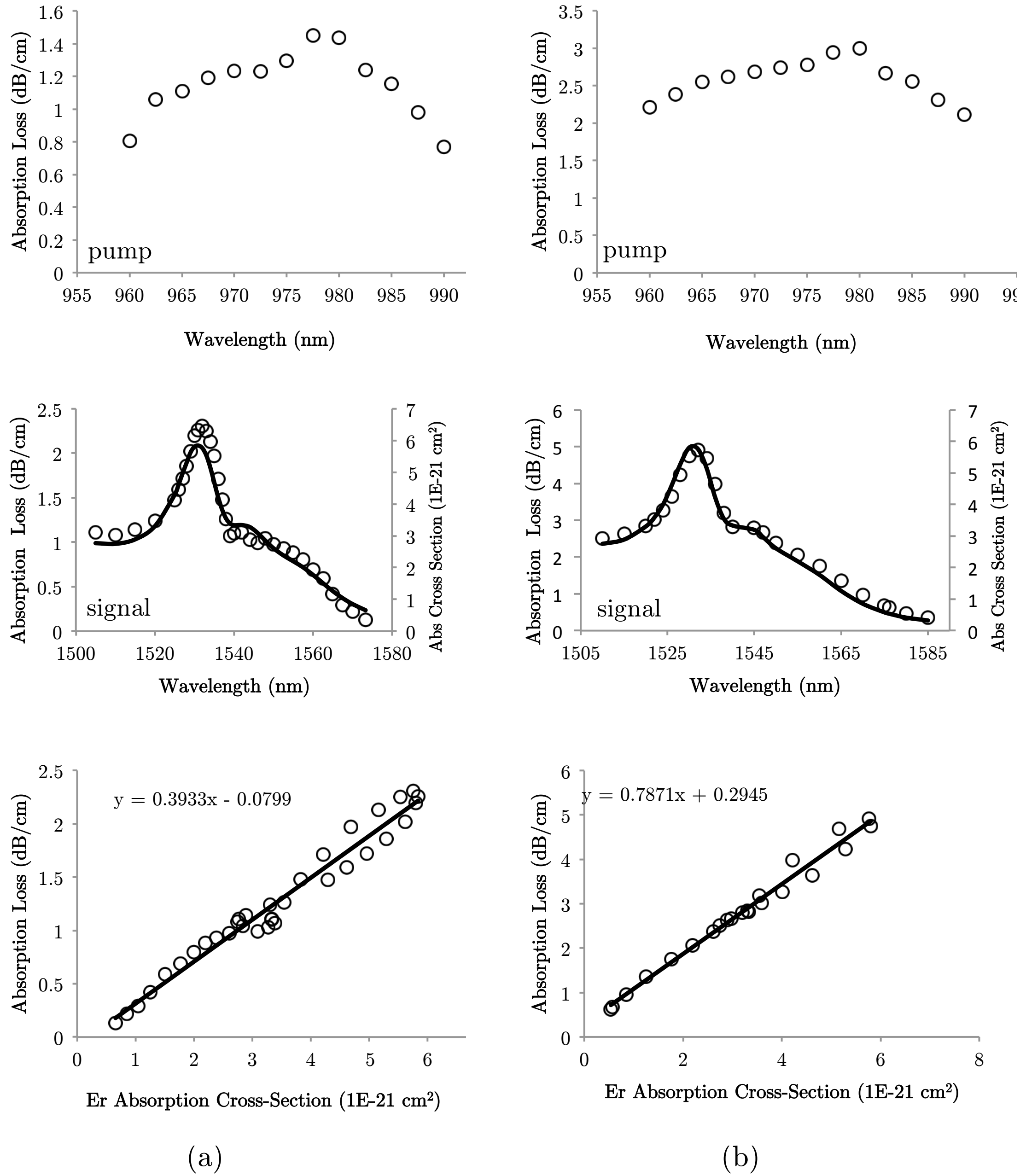

Figure 2.9 – Absorption losses in the pump and signal wavelengths of Er^{3+}:Al_2O_3 films doped with Er^{3+} discharge voltages of (a) 60 V and (b) 75 V. Absorption cross-section data of Er^{3+} [51] is plotted on the secondary vertical axes with the solid line. Concentrations of $9.5x10^{19}$ cm^{-3} and $1.9x10^{20}$ cm^{-3} are obtained from the ratios of losses to the absorption cross-section.

CHAPTER 3

INTEGRATED DISTRIBUTED BRAGG REFLECTOR LASER DESIGN AND OPERATION

3.1 Design Considerations for Optically-Pumped On-Chip Lasers

With increasing demand in high speed interconnects, the use of wavelength division multiplexing (WDM) has become commonplace in optical networks. Invented in the 1970s [75], the WDM technology has been widely studied and is used as a means of increasing communication bandwidth in optical links. Many passive devices making use of the WDM architecture have been demonstrated for use in optical networks, as already shown in Figure 1.4. However, for scalable and low-cost production of these devices, integration using conventional CMOS technologies remains to be the ultimate goal [76].

An on-chip light source is one of the most essential, yet also one of the most difficult to realize components of an integrated WDM photonics link [77]. This is due to silicon's indirect bandgap, which makes light emission extremely challenging in pure silicon devices. However, even with the use of different gain media like doped glasses, several requirements need to be met in order for such a technology to become a scalable standard. These requirements are summarized below.

- **Device footprint:** Since one of the goals of silicon photonics is the full integration of photonic system on centimeter scale die, the laser structures need to occupy a sufficiently small footprint. With the trend towards smaller node sizes in CMOS electronics, photonic structures also need to be properly scaled for compatible packaging and assembly [6]. With a WDM scheme, integration of 8, 16, or 32 laser sources on a single die would require each one of the lasers to have a footprint of approximately 10, 5, and 2 mm^2. At the time of writing, laser sources with footprints smaller than 1 mm^2 can be regarded as a vision that would enable many applications for silicon photonics.

- **Pump confinement in the gain region:** In optically-pumped lasers, the pump laser is absorbed by the gain medium, where the atoms are elevated to an excited state. If pump light is not absorbed, it can be scattered, which ultimately reduces the efficiency of the laser. Therefore, for efficient absorption, confinement of the pump mode within the cross-section of the gain medium is essential. This can be achieved by proper waveguide design and dispersion engineering. However, if the pump and signal wavelengths are significantly far apart, this seemingly simple requirement can be challenging to satisfy. Gain medium confinement of the pump mode will be specifically addressed in later in this chapter.

- **Mode sizes and dopant profile:** Sizes of the pump and signal modes, their overlap, and the distribution of the dopant atoms also influence laser characteristics like pump threshold and laser efficiency. Smaller mode sizes help reduce the threshold pump power as similar levels of pump intensity can be achieved using less power. Another way to achieve higher lasing efficiency is to confine the dopants to the central region of the optical modes where the intensity is highest [78]. This requires one to engineer the on-chip waveguide geometry for maximum possible overlap of the pump and signal modes.

3.2 Design of On-Chip Distributed Bragg Reflector (DBR) Laser

Traditionally, the Bragg condition refers to the phenomenon of constructive interference created by the scattering of light from atoms in a crystalline solid [79]. A similar nomenclature is employed when referring to the interference caused by subsequent reflections from the dielectric boundaries created by a thin film or waveguide geometry. In this section, a laser cavity design that satisfies the above constraints and uses DBRs on either side as reflectors is studied. First, pump and signal mode profiles are solved for various refractive indices of the comprising materials. Then, the design parameters and the spectral response of a DBR are discussed.

3.2.1 Laser Cavity Design

One of the biggest challenges of working with rare-earth dopants results from the inherent constraints of the CMOS fabrication flow. Conventionally, in a silicon-on-insulator (SOI) platform, one can design the waveguide geometry using the 220 nm thick Si layer, and pattern this layer using basic photolithography. However, since rare-earth dopants themselves are not used in CMOS foundries, any materials hosting these dopants also need to be deposited using a back-end process. Ultimately, no further lithography steps are possible after the deposition of any rare-earth doped layers. This requires the underlying layers to be designed in such a way that when the gain medium is blanket deposited on top, the mode confinement, overlap, and dopant profile conditions listed above are satisfied.

For the reactively-sputtered Al_2O_3 described in the previous chapter, refractive indices of 1.60 and 1.58 have been obtained at 980 nm and 1550 nm respectively. For this Al_2O_3 to be the waveguide core, a different medium with a smaller refractive index is needed as the cladding. One possible choice is SiO_2, whose refractive index is approximately 1.45. However, the index contrast between these two media is not large enough to enable sufficiently compact integration. On the other hand, use of Si with Al_2O_3 is also extremely challenging, as the mode would be easily pulled into the Si layer due to Si's much higher refractive index of 3.4. Another possibility is the use of Si_3N_4, whose refractive index is around 2.0. However, the main challenge is then to come up with a waveguide design where the pump and signal modes are guided by Si_3N_4, but are still mainly confined in Al_2O_3.

An appropriate waveguide design is outlined in [80], where a 100 nm thick layer of SiO_2 is used between the 4 μm wide and 100 nm thick guiding Si_3N_4 and the 2 μm thick Al_2O_3 gain medium. This thin layer of SiO_2 acts as a buffer between the two higher index layers, which in turn reduces the guiding tendency of the high index Si_3N_4, and enhances mode confinement in the Al_2O_3 region. An example mode profile for 1550 nm signal inside the laser cavity is given in Figure 3.1. Note that most of the mode is confined in Al_2O_3, whereas lateral confinement and guidance is achieved by the buried Si_3N_4.

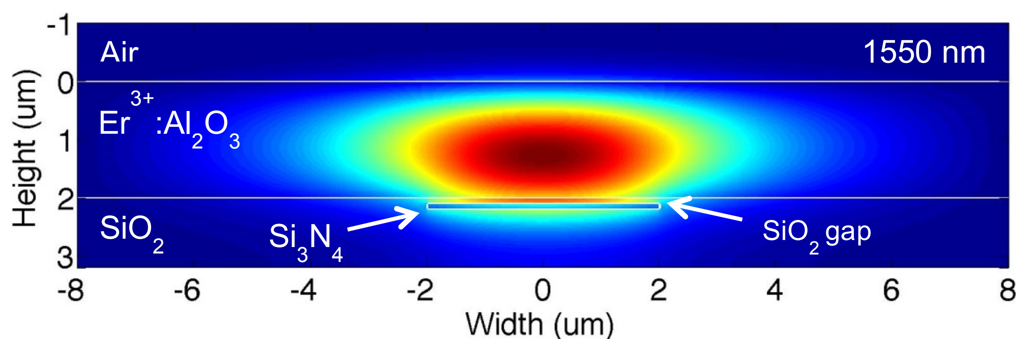

Figure 3.1 – Electric field intensity profile example for waveguide structure described in [80] with 100 nm thick SiO2 gap between Si_3N_4 and Al_2O_3 layers. Buried Si_3N_4 is 4 μm wide and 100 nm thick, and the blanked deposited Al_2O_3 is 2 μm thick.

As expected with glass waveguides' low refractive index contrast, the design shown above is sensitive to changes in the refractive index of the Al_2O_3 layer. Previously, a deposition process almost identical to the one described in [54] was used, which yielded an Al_2O_3 refractive index of 1.65 at 980 nm. However, the process described in the previous chapter was performed in a different sputtering tool, and was optimized under different process conditions, the most important of which is the lower temperature. Therefore, it is natural to expect changes in the refractive index of the resulting materials. In fact, previous research has shown that deposition conditions influence refractive index greatly, as indices anywhere from 1.53 to 1.80 have been recorded for reactively-sputtered Al_2O_3 [81, 82]. Nevertheless, such changes can be accommodated by making slight adjustments to the waveguide design to satisfy the confinement and overlap constraints. These are best analyzed by the intensity distribution profiles obtained with different indices of Al_2O_3 as given in Figures 3.2, 3.3, and 3.4 below. For each mode profile, effective index and mode confinement in Al_2O_3 layer, as well as the mode overlap between the pump and the signal profiles are noted.

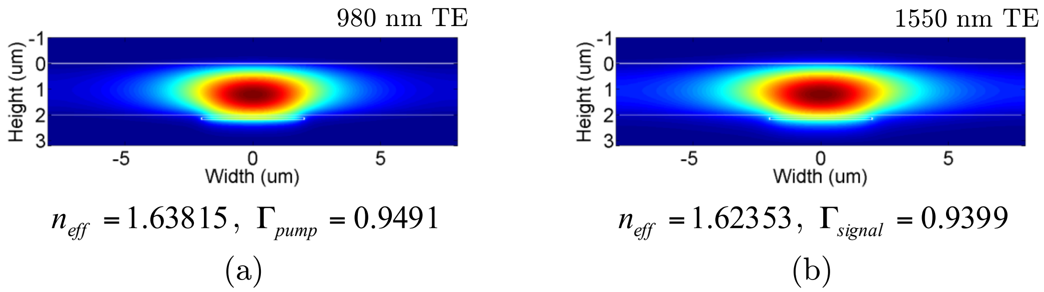

Figure 3.2 – Electric field intensity profiles with Al_2O_3 refractive index of 1.65 for (a) 980 nm fundamental TE pump mode, and (b) 1550 nm fundamental TE signal mode. Excellent pump and signal mode overlap: $\Gamma_{overlap} = 0.9897$

As originally designed for Al_2O_3 refractive index of 1.65, the TE modes for pump and signal wavelengths of 980 nm and 1550 nm are shown in Figure 3.2. Both modes are highly confined in the 2 μm thick Al_2O_3 layer, as indicated by the confinement factors of $\Gamma_{pump} = 0.9491$, and $\Gamma_{signal} = 0.9399$. Consequently, an excellent mode overlap of $\Gamma_{overlap} = 0.9897$ is obtained between the pump and signal modes. This design therefore satisfies the conditions given in Section 3.1.

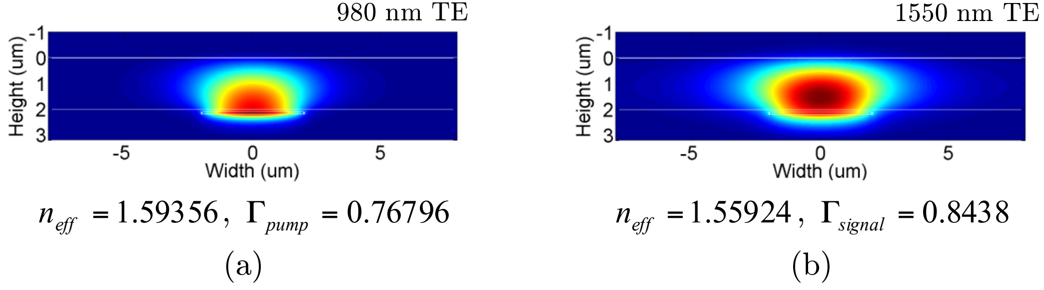

Figure 3.3 – Electric field intensity profiles with lower Al_2O_3 refractive index of (a) 1.60 for 980 nm fundamental TE pump mode, and (b) 1.58 for 1550 nm fundamental TE signal mode. Pump and signal mode overlap is also slightly decreased: $\Gamma_{overlap} = 0.9699$

With the lower refractive index of Al_2O_3, the mode profiles given in Figure 3.3 are obtained. With the refractive index change, the pump mode shape has been altered significantly. The optical mode is now pulled more strongly into the higher index Si_3N_4 layer, as expected. This sensitivity of the pump mode shape is the biggest setback of this design, as a laser with the mode distributions in Figure 3.3 would have a much higher threshold pump power compared with the one in Figure 3.2. On the other hand, the signal mode in Figure 3.3(b) looks fairly similar to the signal mode in Figure 3.2(b). This can be attributed to the longer wavelength of the signal, which plays an important role in determining mode size in a given dielectric geometry. The pump and signal mode overlap is slightly less than before, but still sufficiently high at $\Gamma_{overlap} = 0.9699$. However, the drastic change in the pump mode profile suggests much lower efficiencies from this laser.

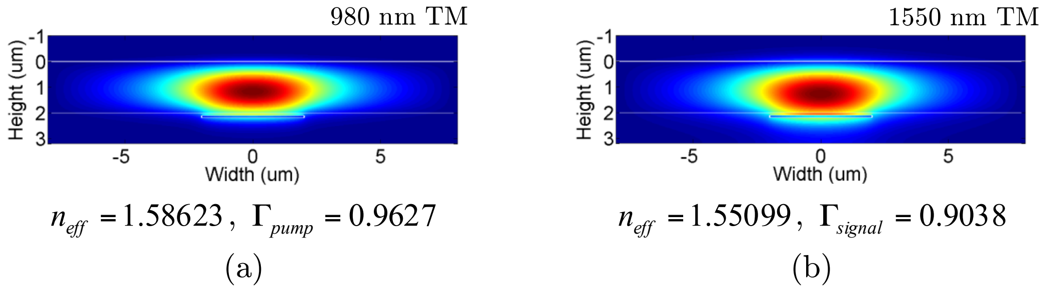

Figure 3.4 – Electric field intensity profiles with lower Al_2O_3 refractive index of (a) 1.60 for 980 nm fundamental TM pump mode, and (b) 1.58 for 1550 nm fundamental TM signal mode. Again, excellent pump and signal mode overlap: $\Gamma_{overlap} = 0.9868$

One way to pull the pump mode back in the Al_2O_3 with the lower refractive index is to use a TM pump. This is easily achieved by the use of a polarization controller. By comparing Figure 3.4(a) and Figure 3.2(a), it can be concluded that the TM pump mode with the lower Al_2O_3 refractive index is in fact similar to the TE pump mode with the higher Al_2O_3 refractive index. The TM pump mode is again highly confined in Al_2O_3, with a confinement factor of $\Gamma_{pump} = 0.9627$. For reference, the TM signal mode is also provided, which is again mostly confined in Al_2O_3. The mode overlap of $\Gamma_{overlap} = 0.9868$ between the TM pump and the TM signal modes is again similar to the TE counterpart in Figure 3.2. This indicates that with the TM pump mode, the constraints given in Section 3.1 can again be satisfied, indicating possible laser operation.

It is important to point out that the waveguide design presented here does not intend to favor either one of the fundamental TE or TM signal modes over one another. However, due to interactions of these fundamental modes with higher order modes or other radiation modes, the fundamental TE and TM modes will inevitably experience different losses inside the laser cavity. In principle, one can solve for the higher order modes and calculate coupling coefficients between the fundamental TE and TM modes to these higher order modes, and find out if one is favored over the other. This requires a much larger simulation window which indicates at least quadratically longer simulation times. In practice, since the output from a laser is usually observed on an optical spectrum analyzer, one can easily determine the lasing wavelength. This can then be used to identify the lasing polarization mode, as cavity gratings have different spectral responses to different polarizations of light. This comes from the difference in the effective indices corresponding to TE and TM signal modes. In the next section, a grating design that makes use of the above described cavity is presented. Using fundamentals of distributed Bragg reflectors, grating responses are simulated for a variety of design parameters.

3.2.2 Spectral Response of Distributed Bragg Reflectors

An integrated DBR is implemented by using materials of alternating refractive indices. Due to successive reflections through alternating dielectric layers, the grating diffracts the forward traveling wave into the backward traveling wave. The resonance of the grating is determined according to the grating period. The Bragg condition for maximum reflection is satisfied when

$$\Lambda = \frac{\lambda_0}{2n_{eff}} \tag{3.1}$$

where Λ is the period of the grating, λ_0 is the vacuum wavelength of light, and n_{eff} is the effective index of the medium that the light propagates in. This effective index is calculated by a 2D mode solver where the refractive index for the grating regions is replaced by an equivalent index n_g calculated from

$${n_g}^2 = (D){n_1}^2 + (1 - D){n_0}^2 \tag{3.2}$$

where n_1 and n_0 are the alternating refractive indices used to make the grating structure, and D is the duty cycle of the grating. Notice that Eq. (3.1) only specifies what wavelength the maximum reflectivity condition will be observed at, and does not provide any other spectral information [27].

The reflectivity itself is determined by the strength of the grating (or equivalently, the coupling coefficient between the forward and backward traveling waves), which depends on a number of factors including the index contrast of the dielectrics that make up the grating, the mode confinement in the grating region, and the duty cycle of the grating. According to coupled mode theory, the coupling coefficient κ is given by

$$\kappa = \frac{{k_0}^2}{2\pi\beta}\left({n_1}^2 - {n_0}^2\right)\sin(\pi D)\Gamma \tag{3.3}$$

where k_0 is the free-space wave vector of light of wavelength λ_0, β is the propagation constant in the grating region, and Γ is how much of the signal mode overlaps with the grating [83]. Note that this is not the same as the mode confinement in the gain medium, as this Γ only refers to the confinement within the part of the cross-section where the mode goes through alternating indices.

Given these parameters, the spectral reflectivity of a uniform Bragg grating of length L is given by

$$r = \frac{\frac{\kappa}{\gamma}\sinh(j\gamma L)}{\cosh(j\gamma L) + \frac{\sigma}{\gamma}\sinh(j\gamma L)} \tag{3.4}$$

where

$$\sigma = \pi\left(\frac{2n_{eff}}{\lambda_0} - \frac{1}{\Lambda}\right)$$
$$\gamma^2 = \sigma^2 - |\kappa|^2 \tag{3.5}$$

are defined for convenience. Example grating response is given in Figure 3.5.

The design parameters described above can be used to engineer a grating's response in the following manner. With an increased coupling strength, the near-flattop response shown in Figure 3.5 (a) is widened even more. This can be used to design wider or narrower filters, as required by the specific application of interest. The coupling strength can be adjusted by changing Γ, which depends on the waveguide geometry. As a result, Γ can be used as a straightforward way of changing filter bandwidth, given that the coupling length L is sufficient. Conversely, the coupling length L can be adjusted in order to raise or lower the maximum reflectivity of the grating, given that the grating has sufficient coupling strength. Examples given in Figure 3.5 demonstrate how Γ and L influence the spectral characteristics of the filter response. Specifically, the effect of reduced coupling strength shown in (b) is compensated by the increased grating length as shown in (c).

In addition to the behavior of the spectral reflectivity around the wavelength at which maximum reflectance is observed, one can also design the grating to have a certain reflectance when the Bragg condition is satisfied. Resonance reflectance can be tuned by adjusting the grating perturbation, a measure of how much the grating differs from a straight waveguide. Although not obviously seen from Eq. (3.4), the grating perturbation influences the mode geometry, which in turn determines n_{eff} and Γ. In the DBR lasers shown in this section, grating reflectivity is tuned by using varying grating perturbation. Here, grating perturbation refers to the length of each tooth of the grating, as shown by the top-down diagram in Figure 3.6. A simulation of grating reflectivity for different perturbation amounts is also given, where increased perturbation strength corresponds to an increase in reflectivity, until the perturbation is strong enough for the reflectivity to saturate around 100%.

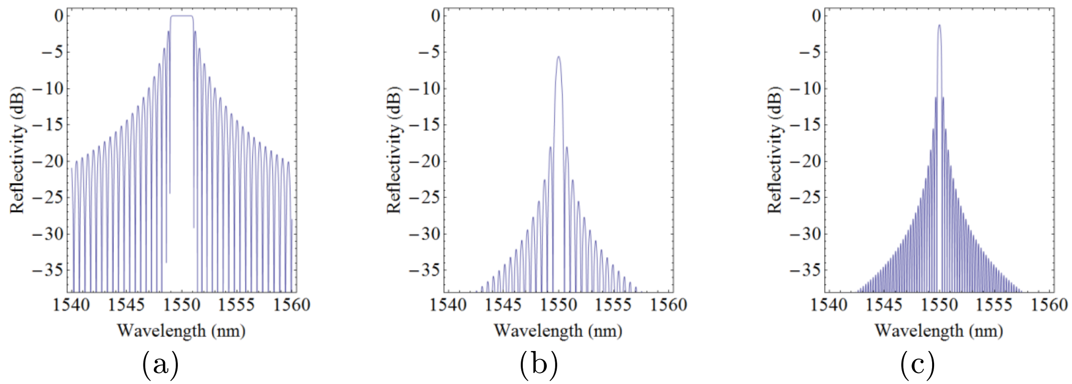

Figure 3.5 – Spectral response of example Bragg gratings with maximum reflectances at around 1550 nm. Responses for (a) reference, (b) reduced coupling strength, and (c) reduced coupling strength but increased coupling length

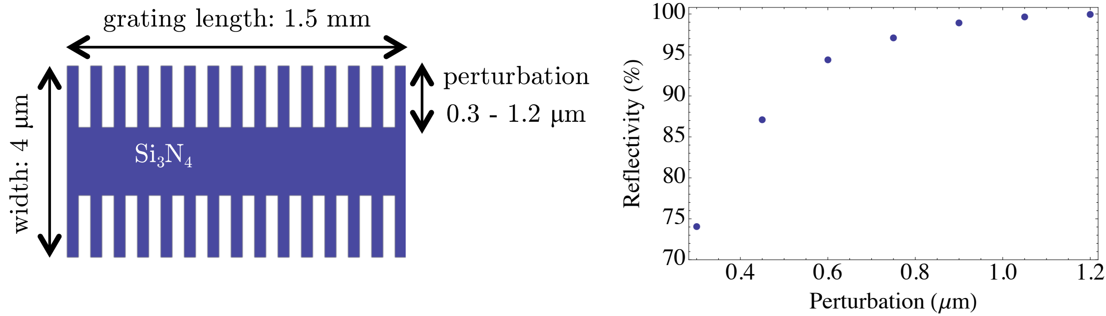

Figure 3.6 – (a) Top-down schematic diagram, and (b) reflectivity as a function of perturbation magnitude for 4 µm wide 100 nm thick Si_3N_4 waveguide with a 100 nm SiO_2 spacing on top, as shown in Figure 3.1.

Of the two gratings on either side of the laser cavity, one of them must be tuned to a slightly lower reflectivity than 100%. The optimal reflectivity depends on the balance between how much light can be allowed to escape the cavity and the intensity of the light remaining inside the laser cavity. Although this can be determined theoretically [19], it requires characterization of the laser cavity, which would necessarily require multiple fabrication runs for characterization and re-optimization of the gratings. Therefore, it is easier to design variations of the same laser with consecutively decreasing grating reflectivities such as 99.5%, 99%, 98%, 96%, 93%, 89%, 85%, and so on. The results given in the following section have been obtained in this manner.

3.3 Fabrication and Measurement of On-Chip DBR Lasers

Now that the proper mode profiles are obtained, and the appropriate Bragg reflector designs are studied, on-chip lasers can be fabricated and tested. Except for the deposition of the gain medium described in Chapter 2, all fabrication steps were done in a standard 300 mm CMOS foundry located in the College of Nanoscale Science and Engineering in University at Albany, State University of New York. The fabrication steps for the waveguide structure shown in Figure 3.1 have been outlined in [80], and can be summarized as follows.

On a standard, blank 300 mm Si wafer, a 6 μm thick layer of SiO_2 was deposited using plasma-enhanced chemical vapor deposition (PECVD). This creates the bottom cladding of the waveguide structure. In order to reduce the scattering losses due to surface roughness, the SiO_2 layer was polished using chemical mechanical polishing (CMP). Then, the Si_3N_4 layer was deposited using PECVD. The Si_3N_4 layer was also polished with CMP in order to reduce surface roughness and to obtain a uniform layer thickness of 100 nm. To reduce mid-IR absorption in Si_3N_4 due to hydrogen bonds incorporated during the PECVD process, the wafer was annealed at 1050 °C for 72 minutes. This plays an important role in reducing cavity losses since Si_3N_4 is the only layer laterally confining the mode. Then, the 100 nm thick Si_3N_4 layer was patterned using 193 nm immersion lithography, and etched using reactive ion etching (RIE) into a 4 μm wide and 20 mm long ridge waveguide. The gratings on either side of the nitride were originally tuned to 1550 nm. To this end, the grating period was determined as $\Lambda = 488\,\text{nm}$ according to Eq. (3.1), and the simulated effective index of $n_{eff} = 1.5881$. $L = 1.5\,\text{mm}$ long gratings with duty cycles of 0.5 were patterned in order to provide sufficient reflectivity. For separate laser structures, grating perturbation was varied from 1.29 μm to 0.45 μm to achieve reflectivities ranging from almost 100% to approximately 85%. After the Si_3N_4 layer has been patterned, the SiO_2 gap was then deposited using PECVD, and again polished by CMP down to 100 nm for surface smoothing and thickness uniformity. Then, in order to easily dice the wafer into individual dies without compromising coupling efficiency, deep dicing trenches were etched using RIE. These trenches are much deeper (at least 50 μm) than any of the nitride layers. This makes it easier to couple light in and out of the die using cleaved fibers, as shown in Figure 3.7. Finally, the 300 mm was diced into 20 x 25 mm dies, the 2 μm thick rare-earth doped gain medium $Er^{3+}:Al_2O_3$ was reactively sputtered on individual dies with an Er^{3+} concentration of $1\text{x}10^{20}$ cm^{-3}, as described in Chapter 2.

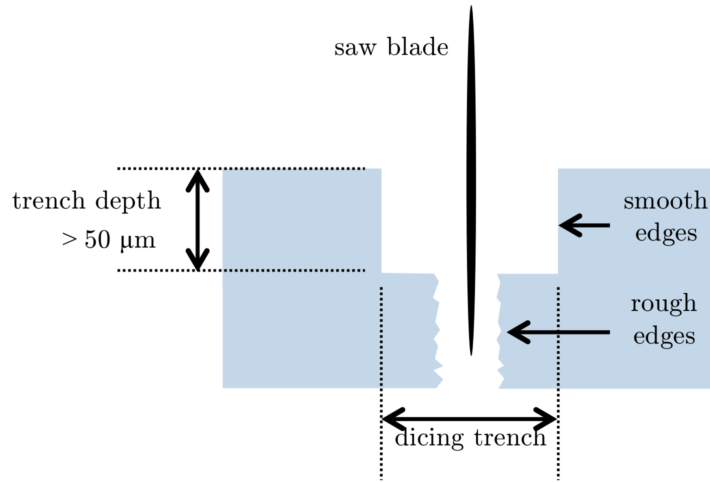

Figure 3.7 – Cross-sectional view of die where dicing saw easily clears the edges of the RIE-etched trenches. Coupling light in and out of on-chip devices is much easier using the smooth facets.

A standard setup was used for measuring laser output. The 20 x 25 mm die was fixed on an optical stage. Cleaved fibers were mounted on 3-axis movable platforms on either side of the die for coupling pump and signal light in and out of the chip. An optical microscope was used for aligning the fibers with the waveguides on the chip. 980 nm pump light was coupled into the laser cavity from either side of the die. Both fibers were polarization controlled, as this was key to the proper operation of the lasers. Signal light was collected from the partially reflected side of the laser cavity, and passed through an external isolator. The collected light was then fed into an optical spectrum analyzer for characterization. The purpose of the external WDM is to isolate the residual 980 nm pump light and only direct the signal light into the spectrum analyzer. A schematic diagram of this setup is presented in Figure 3.8.

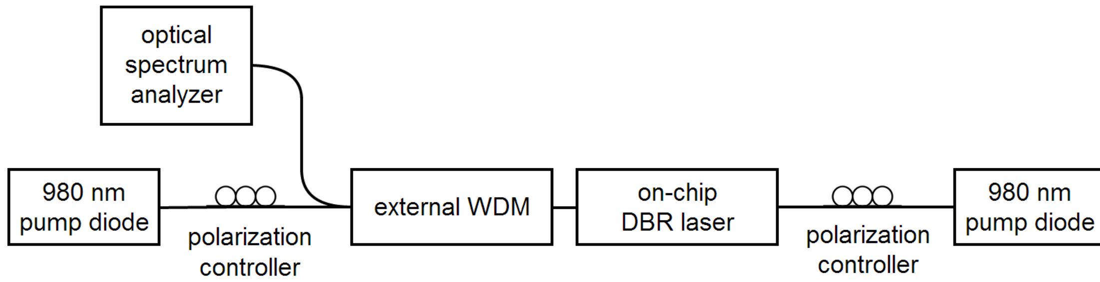

Figure 3.8 – Schematic diagram of laser measurement setup using double sided, polarization controlled 980 nm pumps, and spectrum analyzer for characterization. Laser output is measured from the left side of the on-chip device, where the partially reflecting grating is placed.

In order to accurately measure on-chip power, insertion loss measurements have been carried out to compensate for chip-to-fiber losses. In the 1550 nm range, a coupling loss of 7.3 dB was recorded using an InGaAs photodiode. With this information, spectrum analysis results have been corrected to display on-chip power. Figure 3.9 shows the spectrum analyzer results of a laser output measured in this manner. This specific spectrum was obtained with TM polarized pump light, and with a laser where the partially-reflective DBR grating had a reflectivity of 99%. Since this partially-reflective grating was designed to be on the left of the laser cavity, the laser output was also measured from the left side, as in Figure 3.8.

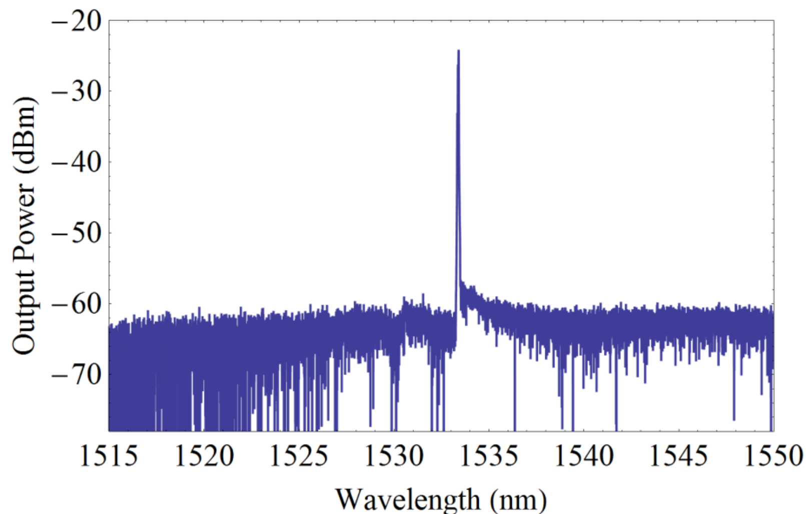

Figure 3.9 – Spectral distribution of on-chip power displaying lasing at 1533.4 nm wavelength with 3.9 µW output power and over 38.9 dB side-mode suppression ratio. Laser cavity was pumped by TM polarized 980 nm light from both sides with a total power of 1.6 W.

According to the optical spectrum analyzer results in Figure 3.9, a maximum on chip power of 3.9 μW (-24.1 dBm) has been recorded at the lasing wavelength of 1533.4 nm. This was achieved when the laser cavity was pumped from both sides using TM polarized 980 nm light. 1.0 A of current was supplied to both of the pump diodes via separate current controllers. Single-mode laser operation is verified, as no other modes of significant power are observed in the lasing spectrum. The noise floor of the spectrum analyzer is also recorded from Figure 3.9 to be around -63 dBm. This yields a side-mode suppression ratio (SMSR) of at least 38.9 dB, indicating the quality of the single-mode lasing operation. This means that any modes that may be recorded in the output of the laser are at least 38.9 dB more suppressed than the primary lasing mode of 1533.4 nm. However, if the output power from the laser was higher, it may have been possible to more accurately determine the SMSR, since modes with higher power would have possibly been detected by the analyzer.

At the beginning of this section, the grating resonance was said to be designed at 1550 nm. One might now ask why the primary lasing output is recorded at 1533.4 nm instead of 1550 nm. This has to do with the previously mentioned decrease in the refractive index of Al_2O_3 from 1.65 to 1.60 in the 1550 nm window. Qualitatively, one can easily trace this refractive index change to an expected resonance shift. With lower refractive index of Al_2O_3, the effective index of a lasing mode in the grating region also decreases. By Eq. (3.1), this results in a blue-shifted resonance in the grating response, as confirmed by the optical spectrum analyzer results. Quantitatively, calculating what the expected resonance requires an iterative method. First, one needs to guess what the new resonance wavelength might be, and solve for the effective index of the mode in the grating region using this initial guess. Using the resultant effective index and the period of the grating, a new resonance wavelength is calculated. This new resonance then becomes the guess for the next iteration of the mode solver. After a four iterations of mode solutions for different polarizations, the resonances have been found to converge to 1532.7862 nm and 1527.1974 nm for fundamental TE and TM modes respectively. This corrected TE mode resonance is much closer to the measured resonance of 1533.4 nm; and the difference is small enough to attribute to fabrication tolerances. This also indicates that the fundamental TM mode is coupled to higher order resonance modes more strongly than the fundamental TE mode. This is verified by plotting the minor electric field components, E_y for TE mode and E_x for TM mode, on a common scale. Although rather non-conventional, plotting minor components clearly indicates unwanted coupling tendencies to higher order modes. Results are shown in Figure 3.10.

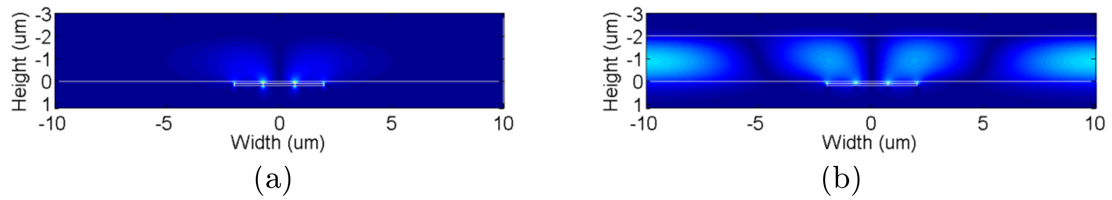

Figure 3.10 – Common scale intensity plots of minor electric field components for different polarizations: (a) E_y for TE mode, and (b) E_x for TM mode.

As indicated by the plots in Figure 3.10, the fundamental TM mode's minor field component is much more spread out than that of the fundamental TE mode. As a result, the TM mode is much more likely to couple into higher order modes and lose intensity as the mode propagates through the waveguide. This again confirms that the lasing mode shown in Figure 3.9 is in fact TE, as also predicted by the resonance response analysis above.

CHAPTER 4

CONCLUSIONS AND OUTLOOK

4.1 Summary and Conclusions

With increasing demand in high speed interconnects, the use of wavelength division multiplexed optical communication systems has become standard in applications with large bandwidth requirements. The field of silicon photonics has emerged in order to realize such systems with silicon-based, CMOS-compatible fabrication techniques. Many of the building blocks of these silicon photonic systems like waveguides, modulators, multiplexers, and detectors have been demonstrated multiple times. However, devices that generate light like amplifiers or lasers have been perhaps the most difficult to affordably fabricate.

Light generation devices using other materials than silicon or other techniques than stimulated absorption have been summarized with their respective advantages and disadvantages. For instance, light sources made of III-V hybrid integrated materials or strained media such as germanium-on-silicon cannot be fabricated using conventional CMOS fabrication methods and require separate epitaxial growth. Raman lasers on the other hand are limited by thermal loading of the crystals, which limit pump powers. As an alternative to these options, rare-earth doped glasses are presented as a gain medium for integrated active optical devices. Since use of similar technologies like the erbium-doped fiber amplifier is well-known in long-distance fiber based communications, the integrated use of rare-earth based gain media is promising.

Because amorphous glass media are easily deposited using physical vapor deposition methods, they can be reliably used as rare-earth hosts in integrated optics. Due to the simplicity of the physical sputtering process and its maturity in the CMOS fabrication flow, low-loss glasses can be consistently sputtered. This consistency is further ensured with an appropriately designed standard operating procedure for a newly purchased sputter tool. With the control of parameters such as temperature, radio-frequency power, oxygen and argon gas flows, and the deposition pressure, a fabrication recipe for low loss Al_2O_3 has been established. Optical losses as low as 0.2 dB/cm at 632 nm, and 0.1 dB/cm for at 1550 nm have been demonstrated in undoped Al_2O_3 films deposited at 250 °C substrate temperature, 400 W of radio-frequency power delivered to an aluminum target, 90 W of radio-frequency power delivered to the substrate, 3.1 sccm of oxygen and 160-110 sccm of argon flow, and 5 mT of process pressure. With the use of substrate bias during deposition, surface roughness of Al_2O_3 films have been reduced from 3.31 nm to 0.35 nm over an area of 1 μm^2 as measured by atomic force microscopy. As a result of the reduced surface roughnesses, for the first time, ultra-low loss Al_2O_3 films have been deposited at temperatures as low as 250°C. This is significant from an integration perspective since increasing temperatures start to compromise

CMOS structural integrity, where significant degradations can occur at temperatures over 500 °C [84].

After the fabrication recipe for undoped Al_2O_3 has been developed, Er^{3+} dopants are incorporated by means of co-sputtering. Absorption losses have been characterized by a prism coupler setup, and Er^{3+} concentrations on the order $1x10^{20}$ cm^{-3} have been achieved with erbium plasma discharge voltages around 65-70 V. The dopant concentration and absorption cross-section data were used to calculate waveguide losses in order to design laser cavities. The cavity was designed with an inverted Si_3N_4 layer for lateral confinement of both the pump and signal modes. Dielectric spacings were designed for the overlap of the modes with the back-end deposited gain medium. With 100 nm Si_3N_4 and 100 nm SiO_2 gap thicknesses, pump and signal mode confinement as well as their overlap with each other was achieved to more than 90%. Although differences in fabrication equipment resulted in a slightly lower refractive index of 1.60 for Al_2O_3 than the designed value of 1.65, the difference was mitigated by the use of TM polarized pump, where mode confinement and overlap factors were again over 90%.

Distributed Bragg reflectors were placed on either side of the laser cavity. Grating resonance was modeled using the effective index of the signal mode along with the geometrical structure of the dielectrics. With 1.5 mm long Si_3N_4-SiO_2 gratings, sidewall perturbation was varied from 1.29 μm to 0.45 μm to achieve reflectivities ranging from almost 100% down to about 85%. After the fabrication of the devices in a standard 300 mm CMOS foundry, Er^{3+}:Al_2O_3 gain medium was reactively sputtered with the 250 °C process developed here. Laser output was measured using a standard setup with double-sided 980 nm pump lasers and an optical spectrum analyzer. 3.9 μW of on-chip optical power was recorded with single mode lasing at the wavelength of 1533.4 μm. Side mode suppression ratio of 38.9 dB was achieved, although this quantity was limited by the noise floor of the optical spectrum analyzer. This marks the first demonstration of a working on-chip C-band laser with a rare-earth gain medium deposited as low as 250 °C.

4.2 Future Work and Outlook

In order to describe possible directions for future work, the issues with the existing system need to be revisited. Listed below are a few outstanding problems with proposed solutions.

Due to system losses through passive elements, most optical communication systems need on-chip signal powers around 1 mW. Our aim here however was to show that low temperature (250 °C) deposited Er^{3+}:Al_2O_3 can be used as a

potential gain medium for silicon photonics. As explained with mode profiles in Chapter 3, the lasers were originally designed for TE polarized pumping, where TM polarized pump had to be used since the refractive index of Al_2O_3 was lower than the value the laser cavity was designed for. An obvious next step is then to change the process parameters in order to achieve a greater refractive index, assuming that the laser design is not altered due to fabrication costs. Another method to increase luminescence intensity is through the use of co-dopants such as Yb^{3+}. Due to the tendency of Er^{3+} ions to cluster, the lasing upper state lifetime is reduced and light emission is quenched [46]. Previous studies have shown that by efficient energy transfer mechanisms between Yb^{3+} and Er^{3+} ions, luminescence quenching can be significantly reduced [47,57]. Yb^{3+} and Er^{3+} codoping can help achieve higher on-chip optical powers that are needed by WDM integrated systems. Moreover, other rare-earth dopants such as neodymium (Nd^{3+}), thulium (Tm^{3+}), and holmium (Ho^{3+}) can be used instead of Er^{3+} for lasing wavelengths from near to far infrared [85]. Possible use of the whole infrared spectrum can be extremely beneficial in non-linear optical applications such as frequency comb generation.

The refractive index problem discussed here stems from the fact that glasses like alumina do not provide much index contrast with the surrounding layers of glasses. For instance, SiO_2, Al_2O_3, and Si_3N_4 have refractive indices of 1.45, 1.65, 1.99 respectively. Phosphate and fluoride glasses also have indices varying between 1.4 and 1.6. In addition to low integration density, devices designed using low index contrast materials are sensitive to slight changes in these indices. It is also well known that slight differences in the fabrication procedure or the transfer of the process from one tool to another can change the refractive index of the resulting material. Therefore, potential use of silicon can help mitigate the issue of device sensitivity due to silicon's high refractive index of 3.4. However, as mentioned in Chapter 3, rare-earth dopants are not easily soluble in silicon. A possible design can make use of a slot mode waveguide made from doped glass and surrounded by silicon channels. Channels of appropriate width and thickness can be easily patterned onto an SOI wafer and similarly back-end deposited with doped glasses. This would allow for utilization of high index contrast made possible by silicon.

The process developed here does not have to be limited to active devices. A similar sputtering recipe can be created for other oxides such as SiO_2 or TiO_2 to be used in their undoped forms in silicon photonic circuits. For instance, TiO_2 is of particular interest due to its negative thermo-optic coefficient, which results in its refractive index to decrease with increasing temperature. Resonators making use of this effect have already been designed in order to achieve a resonance peak that is independent of temperature [86,87]. These "athermal" resonators play an important role in the frequency stabilization of

laser systems [88]. With the fabrication scheme developed here, a combination of positive and negative thermo-optic coefficient materials like Al_2O_3 and TiO_2 can be deposited in layers, which can help not only stabilize the resonance wavelength, but also reduce the thermal noise of an integrated resonator.

These applications show the promise of the techniques developed in this thesis and how they can be utilized to realize a new set of low-temperature deposited, CMOS-compatible devices. With this new set of devices and enhanced integration capabilities, a fully integrated on-chip silicon photonics link can be demonstrated and used as an answer to our ever-growing need for high bandwidth information access.

REFERENCES

[1] Shockley, William. ”Circuit element utilizing semiconductive material.” U.S. Patent No. 2,569,347. 25 Sep. 1951.

[2] Price, Robert W. *Roadmap to entrepreneurial success: Powerful strategies for building a high-profit business*. AMACOM Div American Mgmt Assn, 2004.

[3] Chen, F., et al. ”Line edge roughness and spacing effect on low-k TDDB characteristics.” Reliability Physics Symposium, 2008. IRPS 2008. IEEE International. IEEE, 2008.

[4] Chen, X., et al. ”A cost effective 32nm high-K/metal gate CMOS technology for low power applications with single-metal/gate-first process.” VLSI Technology, 2008 Symposium on. IEEE, 2008.

[5] Jan, C-H., et al. ”A 32nm SoC platform technology with 2 nd generation high-k/metal gate transistors optimized for ultra low power, high performance, and high density product applications.” *Electron Devices Meeting (IEDM), 2009 IEEE International*. IEEE, 2009.

[6] International Technology Roadmap for Semiconductors. ”2012 Overall Roadmap Technology Characteristics.” *ITRS Technology Trend Targets.* Web.

[7] Ahmed, Khaled, and Klaus Schuegraf. ”Transistor wars.” *Spectrum, IEEE* 48.11 (2011): 50-66.

[8] Sutter, Herb. ”The free lunch is over: A fundamental turn toward concurrency in software.” *Dr. Dobb's Journal* 30.3 (2005): 202-210.

[9] Danowitz, Andrew, et al. ”CPU DB: recording microprocessor history. ”*Communications of the ACM* 55.4 (2012): 55-63.

[10] ”ARK — Intelff Pentiumff D Processor 820 (2M Cache, 2.80 GHz, 800 MHz FSB).” *ARK Product Launch.* Intel Corporation, 4 Aug. 2013. Web. 12 Apr. 2014. http://ark.intel.com/products/27512/.

[11] Su, Zhan. *Polarization manipulation in silicon photonics.* Master's thesis. Massachusetts Institute of Technology, 2013.

[12] Lau, John H. ”Ball grid array technology.” (1995): 565-591.

[13] Lee, Benjamin G., et al. ”Ultrahigh-bandwidth silicon photonic nanowire waveguides for on-chip networks.” *Photonics Technology Letters, IEEE* 20.6 (2008): 398-400.

[14] Mattis, D. C., and John Bardeen. ”Theory of the anomalous skin effect in normal and superconducting metals.” *Physical Review* 111.2 (1958): 412.

[15] Shin, Jaemin, et al. ”Rapid, predictive measurement-based modeling for high frequency interconnect on FR4 substrate.” *Electronic*

Components and Technology Conference, 2005. Proceedings. 55th. IEEE, 2005.

[16] Senthinathan, R., and J. L. Prince. "Simultaneous switching ground noise calculation for packaged CMOS devices." *Solid-State Circuits, IEEE Journal of* 26.11 (1991): 1724-1728.

[17] Allen, Rick. "NVIDIA Unleashes Highest Performance DirectX 10 GPU for Notebooks." *Visual Computing Leadership from NVIDIA.* NVIDIA, 1 Jan. 2013. Web. 18 Mar. 2014. http://www.nvidia.com.

[18] Tummala, Rao R. "Moore's law meets its match (system-on-package)."*Spectrum, IEEE* 43.6 (2006): 44-49.

[19] Saleh, Bahaa E. A., and Malvin Carl Teich. *Fundamentals of photonics.* 2nd ed. Hoboken, N.J.: Wiley-Interscience, 2007.

[20] Whitehouse, David. "World's oldest telescope? " *BBC News.* BBC, 7 Jan. 1999. Web. 10 Apr. 2014. http://news.bbc.co.uk.

[21] Magden, Emir Salih. *Effects of Strain Release via Interfacial Misfit Arrays on The Optical Properties of GaAs/GaSb Heterojunctions.* Senior thesis. Tufts University, 2012.

[22] Schawlow, Arthur L., and Charles H. Townes. "Infrared and optical masers."*Physical Review* 112.6 (1958): 1940

[23] Gould, R. Gordon. "The LASER, light amplification by stimulated emission of radiation." *The Ann Arbor conference on optical pumping, the University of Michigan.* Vol. 15. 1959.

[24] Kao, K. C., and George A. Hockham. "Dielectric-fibre surface waveguides for optical frequencies." *Electrical Engineers, Proceedings of the Institution of*113.7 (1966): 1151-1158.

[25] Keck, D. Us, and P. Us Schultz. "Method of producing optical waveguide fibers." U.S. Patent No. 3,711,262. 16 Jan. 1973.

[26] Jewell, Jack L., et al. "Vertical-cavity surface-emitting lasers-design, growth, fabrication, characterization." *IEEE Journal of Quantum Electronics* 27 (1991): 1332-1346.

[27] Sun, Jie. *Toward accurate and large-scale silicon photonics.* Doctoral thesis. Massachusetts Institute of Technology, 2013.

[28] Dong, Po, et al. "Low Vpp, ultralow-energy, compact, high-speed silicon electro-optic modulator." *Optics Express* 17.25 (2009): 22484-22490.

[29] Baldwin, J. "A wave of integration." *Electronics Letters* 49.6 (2013): 377-377.

[30] "Silicon waveguide cleans up optical signals." *Silicon waveguide cleans up optical signals.* SPIE, 12 Dec. 2007. Web. 4 May 2014. http://optics.org.

[31] Alduino, Andrew, et al. "Demonstration of a high speed 4-channel integrated silicon photonics WDM link with hybrid silicon lasers." *Integrated Photonics Research, Silicon and Nanophotonics.* Optical Society of America, 2010.

[32] Jalali, Bahram. "Making silicon lase." *Scientific American* 296.2 (2007): 58-65.
[33] Fang, Alexander W., et al. "Electrically pumped hybrid AlGaInAs-silicon evanescent laser." *Optics Express* 14.20 (2006): 9203-9210.
[34] Ben Bakir, B., et al. "Electrically driven hybrid Si/III-V Fabry-Pérot lasers based on adiabatic mode transformers." *Optics express* 19.11 (2011): 10317-10325.
[35] Sun, Xiaochen, et al. "Direct gap photoluminescence of n-type tensile-strained Ge-on-Si." *Applied Physics Letters* 95.1 (2009): 011911.
[36] Liu, Jifeng, et al. "Ge-on-Si laser operating at room temperature." *Optics letters*35.5 (2010): 679-681.
[37] Rong, Haisheng, et al. "A cascaded silicon Raman laser." *Nature photonics* 2.3 (2008): 170-174.
[38] Pask, H. Ml. "The design and operation of solid-state Raman lasers." *Progress in Quantum Electronics* 27.1 (2003): 3-56.
[39] Lombardo, S., et al. "Room-temperature luminescence from Er-implanted semi-insulating polycrystalline silicon." *Applied physics letters* 63.14 (1993): 1942-1944.
[40] Fujii, Minoru, et al. "1.54 μm photoluminescence of Er3+ doped into SiO2 films containing Si nanocrystals: evidence for energy transfer from Si nanocrystals to Er3+." *Applied Physics Letters* 71.9 (1997): 1198-1200.
[41] Han, Hak-Seung, Se-Young Seo, and Jung H. Shin. "Optical gain at 1.54 μm in erbium-doped silicon nanocluster sensitized waveguide." *Applied Physics Letters* 79.27 (2002): 4568-4570.
[42] Mears, R. J., et al. "Low-noise erbium-doped fibre amplifier operating at 1.54 μm." *Electronics Letters* 23.19 (1987): 1026-1028.
[43] Becker, Philippe M., Anders A. Olsson, and Jay R. Simpson. *Erbium-doped fiber amplifiers: fundamentals and technology*. Academic press, 1999.
[44] Paschotta, Rüdiger. *Encyclopedia of laser physics and technology*. Vol. 1. Berlin: Wiley-vch, 2008.
[45] Bradley, Jonathan DB, et al. "Monolithic erbium-and ytterbium-doped microring lasers on silicon chips." *Optics Express* 22.10 (2014): 12226-12237.
[46] Delevaque, E., et al. "Modeling of pair-induced quenching in erbium-doped silicate fibers." *Photonics Technology Letters, IEEE* 5.1 (1993): 73-75.
[47] Ding, Ming, and Peter K. Cheo. "Effects of Yb: Er-codoping on suppressing self-pulsing in Er-doped fiber lasers." *Photonics Technology Letters, IEEE* 9.3 (1997): 324-326.

[48] Gan, Fuxi. "Optical properties of fluoride glasses: a review." *Journal of non-crystalline solids* 184 (1995): 9-20.

[49] Jiang, Shibin, et al. "Er^{3+}-doped phosphate glasses for fiber amplifiers with high gain per unit length." *Journal of non-crystalline solids* 263 (2000): 364-368.

[50] Davis, K. Miura, et al. "Writing waveguides in glass with a femtosecond laser." *Optics letters* 21.21 (1996): 1729-1731.

[51] Barnes, William L., et al. "Absorption and emission cross section of Er 3+ doped silica fibers." *Quantum Electronics, IEEE Journal of* 27.4 (1991): 1004-1010.

[52] Sigmund, Peter. "Theory of sputtering. I. Sputtering yield of amorphous and polycrystalline targets." *Physical review* 184.2 (1969): 383.

[53] Mahnke, M., et al. "Aluminum oxide doped with erbium, titanium and chromium for active integrated optical applications." *AEU-International Journal of Electronics and Communications* 55.5 (2001): 342-348.

[54] Worhoff, Kerstin, et al. "Reliable Low-Cost Fabrication of Low-Loss Waveguides With 5.4-dB Optical Gain." *Quantum Electronics, IEEE Journal of* 45.5 (2009): 454-461.

[55] Sheng, Lie-yi, et al. "A low-power CMOS compatible integrated gas sensor using maskless tin oxide sputtering." *Sensors and Actuators B: Chemical* 49.1 (1998): 81-87.

[56] Sedky, Sherif, et al. "Experimental determination of the maximum post-process annealing temperature for standard CMOS wafers." *Electron Devices, IEEE Transactions on* 48.2 (2001): 377-385.

[57] Strohhöfer, Christof, and Albert Polman. "Absorption and emission spectroscopy in Er^{3+}–Yb^{3+} doped aluminum oxide waveguides." *Optical Materials* 21.4 (2003): 705-712.

[58] Lifshitz, Y., G. D. Lempert, and E. Grossman. "Substantiation of subplantation model for diamondlike film growth by atomic force microscopy." *Physical review letters* 72.17 (1994): 2753.

[59] Egermeier, John C., Xin Guo, and Mark A. Mueller. "Method for in-situ cleaning a Ti target in a Ti+ TiN coating process." U.S. Patent No. 5,427,666. 27 Jun. 1995.

[60] Berg, Sören, and Tomas Nyberg. "Fundamental understanding and modeling of reactive sputtering processes." *Thin solid films* 476.2 (2005): 215-230.

[61] Combadiere, L., and J. Machet. "Study and control of both target-poisoning mechanisms and reactive phenomenon in reactive planar magnetron cathodic sputtering of TiN." *Surface and Coatings Technology* 82.1 (1996): 145-157.

[62] Kelly, P. J., and R. D. Arnell. "Control of the structure and properties of aluminum oxide coatings deposited by pulsed magnetron sputtering." *Journal of Vacuum Science & Technology A* 17.3 (1999): 945-953.

[63] Berg, S., T. Larsson, and H-O. Blom. "The use of nitrogen flow as a deposition rate control in reactive sputtering." *Journal of Vacuum Science & Technology A*4.3 (1986): 594-597.

[64] Depla, Diederik, et al. "Hysteresis behavior during reactive magnetron sputtering of Al_2O_3 using a rotating cylindrical magnetron." *Journal of Vacuum Science & Technology A* 24.4 (2006): 934-938.

[65] Sproul, William D. "High rate reactive sputtering process control." *Surface and Coatings Technology* 33 (1987): 73-81.

[66] Serikawa, T., and A. Okamoto. "Effect of N_2-Ar mixing on the reactive sputtering characteristics of silicon." *Thin Solid Films* 101.1 (1983): 1-6.

[67] Okamoto, A., and T. Serikawa. "Reactive sputtering characteristics of silicon in an Ar-N_2 mixture." *Thin Solid Films* 137.1 (1986): 143-151.

[68] Suhail, M. H., G. Mohan Rao, and S. D. C. J. Mohan. "dc reactive magnetron sputtering of titanium-structural and optical characterization of TiO2 films."*Journal of Applied Physics* 71.3 (1992): 1421-1427.

[69] Meng, Li-Jian, and M. P. Dos Santos. "Investigations of titanium oxide films deposited by dc reactive magnetron sputtering in different sputtering pressures."*Thin Solid Films* 226.1 (1993): 22-29.

[70] Löbl, P., M. Huppertz, and D. Mergel. "Nucleation and growth in TiO_2 films prepared by sputtering and evaporation." *Thin solid films* 251.1 (1994): 72-79.

[71] Metricon Corporation. "Model 2010/M Basic Description.",1 Jan. 2010. Web. 19 Jan. 2014. www.metricon.com.

[72] Li, Quan, et al. "Low-temperature magnetron sputter-deposition, hardness, and electrical resistivity of amorphous and crystalline alumina thin films." *Journal of Vacuum Science & Technology A* 18.5 (2000): 2333-2338.

[73] Koski, Kari, Jorma Hölsä, and Pierre Juliet. "Properties of aluminium oxide thin films deposited by reactive magnetron sputtering." *Thin Solid Films* 339.1 (1999): 240-248.

[74] Borselli, Matthew, et al. "Rayleigh scattering, mode coupling, and optical loss in silicon microdisks." *Applied Physics Letters* 85.17 (2004): 3693-3695.

[75] DeLange, OWEN E. ”Wide-band optical communication systems: Part II—Frequency-division multiplexing.” *Proceedings of the IEEE* 58.10 (1970): 1683-1690.
[76] Won, Rachel, and Mario Paniccia. ”Integrating silicon photonics.” Nature Photonics (2010): 498-499.
[77] Editorial. “Simply silicon” Nature Photonics (2010): 491.
[78] Giles, C. Randy, and Emmanuel Desurvire. ”Modeling erbium-doped fiber amplifiers.” *Lightwave Technology, Journal of* 9.2 (1991): 271-283.
[79] Pedrotti, Frank L., Leno S. Pedrotti, and Leno S. Pedrotti. *Introduction to optics*. Vol. 2. Englewood Cliffs: Prentice-Hall, 1993.
[80] Purnawirman, et al. ”C-and L-band erbium-doped waveguide lasers with wafer-scale silicon nitride cavities.” *Optics letters* 38.11 (2013): 1760-1762.
[81] Shimada, M., et al. ”Ultrathin Al_2O_3 and AlN films deposited by reactive sputter using advanced electron cyclotron resonance plasma source.” *Vacuum* 59.2 (2000): 727-734.
[82] Seino, T., and T. Sato. ”Aluminum oxide films deposited in low pressure conditions by reactive pulsed dc magnetron sputtering.” *Journal of Vacuum Science & Technology A* 20.3 (2002): 634-637.
[83] Murphy, Thomas E. *Design, fabrication and measurement of integrated Bragg grating optical filters*. Doctoral thesis. Massachusetts Institute of Technology, 2000.
[84] Sedky, Sherif, et al. ”Experimental determination of the maximum post-process annealing temperature for standard CMOS wafers.” *Electron Devices, IEEE Transactions on* 48.2 (2001): 377-385.
[85] Aggarwal, Ishwar D., et al. ”Infrared transparent selenide glasses.” U.S. Patent No. 5,846,889. 8 Dec. 1998.
[86] Alipour, Payam, et al. ”Titania-clad microresonators on SOI with athermal performance.” *Conference on Lasers and Electro-Optics*. Optical Society of America, 2010.
[87] Guha, Biswajeet, Jaime Cardenas, and Michal Lipson. ”Athermal silicon microring resonators with titanium oxide cladding.” *Optics express* 21.22 (2013): 26557-26563.
[88] Drever, R. W. P., et al. ”Laser phase and frequency stabilization using an optical resonator.” *Applied Physics B* 31.2 (1983): 97-105.